Lithos 266–267 (2016) 115–132

Contents lists available at ScienceDirect

Lithos

journal homepage: www.elsevier.com/locate/lithos

Geochronology and Geochemistry of Igneous Rocks from the Laoshankou District, North Xinjiang: Implications for the Late Paleozoic Tectonic Evolution and Metallogenesis of East Junggar

Pei Liang [a,b], Huayong Chen [a,*], Pete Hollings [c], Chao Wu [a,b], Bing Xiao [a,b], Zhiwei Bao [a], Deru Xu [a]

[a] Key Laboratory of Mineralogy and Metallogeny, Guangzhou Institute of Geochemistry, Chinese Academy of Sciences, 511 Kehua Road, Guangzhou, 510640, China
[b] Graduate University of Chinese Academy of Sciences, 19 Yuquan Road, Beijing, 100049, China
[c] Department of Geology, Lakehead University, 955 Oliver Road, Thunder Bay, Ontario, P7B5E1, Canada

ARTICLE INFO

Article history:
Received 15 November 2015
Accepted 18 August 2016
Available online 28 August 2016

Keywords:
Geochemistry
Igneous rocks
Island arc environment
Late Paleozoic
Laoshankou district
East Junggar

ABSTRACT

The Fe-Cu mineralization of the Laoshankou district is located in the Dulate Late Paleozoic island arc at the northern margin of East Junggar terrane, Northwest China and is hosted by volcanic rocks of the Middle Devonian Beitashan Formation. LA-ICP-MS U–Pb dating of zircon constrains the timing of crystallization of biotite diorites and quartz syenites in the Laoshankou district to 379 ± 2 Ma and 376 ± 2 Ma, respectively.

The volcanic rocks are calc-alkaline in composition and are characterised by LILE and LREE enrichments and HFSE depletions, consistent with a subduction-related affinity. The relatively depleted Nb, Ta, Zr, Hf and Th, enriched Sr and Ba, elevated Mg#, positive $\varepsilon_{Nd}(t)$ values (5.5 and 5.6), low $(^{87}Sr/^{86}Sr)_i$ ratios (0.7042 and 0.7044) and MORB-like Pb-isotope characters all suggest that they were derived from a depleted mantle wedge metasomatized by slab-derived fluids, without crustal contamination. The biotite diorite shows slightly metaluminous compositions and is geochemically similar to the volcanic rocks, suggesting that they were derived from the same depleted mantle source. The lack of correlation between SiO_2 and initial Sr, Nd ratios suggests that fractional crystallization dominated the petrogenesis of the biotite diorite with only weak crustal contamination. The geochemical characteristics of the quartz syenite are distinct from the volcanic rocks and the biotite diorite. The positive $\varepsilon_{Hf}(t)$, $\varepsilon_{Nd}(t)$, high Th/La (0.17–0.53), Th/Yb (1.62–4.39), low Ce/Th (2.87–10.13) ratios and positive trends of SiO_2 versus $(^{87}Sr/^{86}Sr)_i$ and $(^{143}Nd/^{144}Nd)_i$ indicate the quartz syenite is likely the product of a depleted mantle wedge metasomatized by slab-derived fluids and subducted sediment-derived melts that underwent crustal contamination during passage through the crust.

The low abundance of Th, Yb, Ta and La, indicate that all the intrusive rocks from 379 to 376 Ma in the Laoshankou district formed in an island arc rather than a continental margin arc. The northern margin of East Junggar was related to the southward subduction of the Kuerti-Erqis Ocean (a branch of the Paleo-Asian Ocean) between the Altay and the Dulate arcs in this period, consistent with the presence of Nb-enriched basalts and boninites in the north of the Dulate arc and the island arc rather than back arc setting of the igneous rocks in the Laoshankou district.

For metallogenesis in the northern margin of East Junggar, arc-related Fe-Cu-Au and porphyry Cu mineralization was dominated. There is large potential to find several Late Paleozoic arc-related Fe-Cu-Au mineralizations in North Xinjiang.

1. Introduction

The Central Asian Orogenic Belt (CAOB; Fig. 1a), the largest Paleozoic to Mesozoic accretionary orogeny in the world, is situated between two major Precambrian cratons: the Siberian to the north and the North China-Tarim to the south and extends from the Urals in the west to the Pacific Ocean in the east. The belt contains numerous tectonic units including island arcs, ophiolites, accretionary complexes, oceanic plateaus, and continental blocks or microcontinents (Huang et al., 2014; Jahn et al., 2000; Sun et al., 2008; Wang et al., 2006; Windley et al., 2002; Xiao et al., 2008). Since the 1990s, the CAOB has been the subject of considerable study as it is critical to the understanding of the development of accretionary orogenies in central Asia. However, the allochthonous nature of many of the terranes and their complicated collisional history make unraveling the tectonic evolution of the CAOB difficult. A number of models have been proposed to explain the development of the area, including (1) successive accretion of the long-lived Kipchak-Tuva-Mongol arc (Sengor and Natalin, 1996; Sengor et al., 1993); (2) the accretion-collision of multiple-subduction systems,

* Corresponding author.
E-mail address: huayongchen@gig.ac.cn (H. Chen).

http://dx.doi.org/10.1016/j.lithos.2016.08.021
0024-4937/

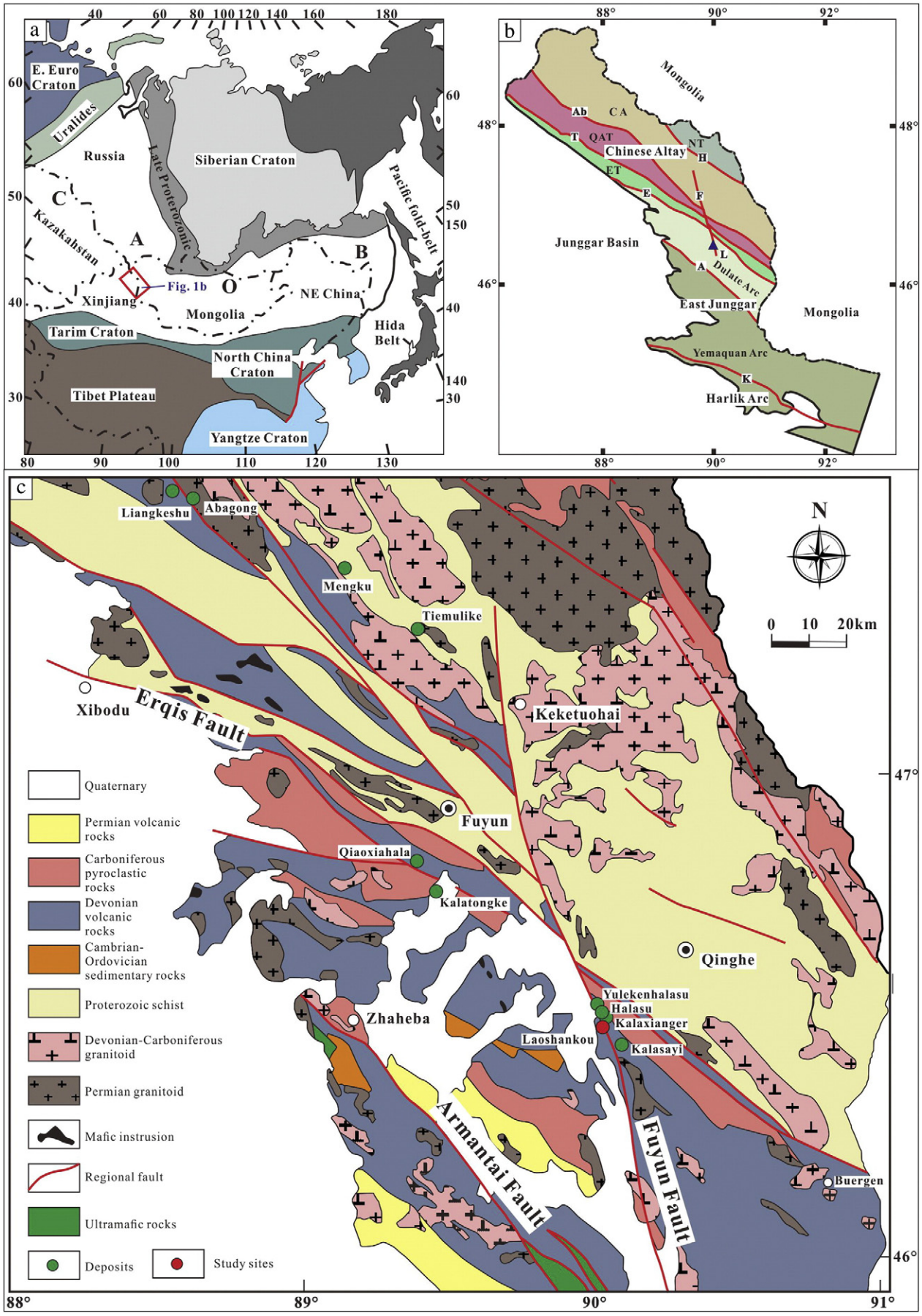
a
E. Euro Craton
Uralides
Russia
Late Proterozoic
Siberian Craton
Pacific fold-belt
Kazakahstan
C
A
B
O
Fig. 1b
Xinjiang
NE China
Mongolia
Tarim Craton
Hida Belt
North China Craton
Tibet Plateau
Yangtze Craton
b
Mongolia
Ab
CA
T
QAT
Chinese Altay
NT
H
ET
E
F
Junggar Basin
L
A
Dulate Arc
East Junggar
Mongolia
Yemaquan Arc
K
Harlik Arc
c
Liangkeshu
Abagong
Mengku
Tiemulike
N
0 10 20km
Xibodu
Erqis Fault
Keketuohai
Quaternary
Permian volcanic rocks
Carboniferous pyroclastic rocks
Devonian volcanic rocks
Cambrian-Ordovician sedimentary rocks
Proterozoic schist
Devonian-Carboniferous granitoid
Permian granitoid
Mafic instrusion
Regional fault
Ultramafic rocks
Deposits
Study sites
Fuyun
Qiaoxiahala
Kalatongke
Qinghe
Yulekenhalasu
Halasu
Kalaxianger
Zhaheba
Laoshankou
Kalasayi
Armantai Fault
Fuyun Fault
Buergen
88°
89°
90°
91°
47°
46°

similar to the present-day SW Pacific archipelago (Sun et al., 2008; Windley et al., 2002) and (3) fore-arc accretion punctuated by opening and closing of back-arc basins (Long et al., 2012; Yakubchuk, 2004). In order to develop a better understanding of the history of the CAOB, these models need to be tested and augmented with new geochemical data.

The Junggar block, in the central-north part of the CAOB, is one of the largest terranes in the belt and traditionally has been divided into the East Junggar, the West Junggar and the Junggar Basin (Fig. 1b). The East Junggar terrane is located in the northeast of the Junggar block. Over the past several decades, considerable research has been undertaken to clarify the tectonic evolution of the East Junggar and concluded that it is closely associated with the evolution of the Paleo-Asian Ocean. Despite significant advances, some critical problems remain unsolved, including two main issues: (1) whether the tectonic setting of the northern margin of East Junggar in the Late Paleozoic was an island arc (Windley et al., 2002; Zhang et al., 2009) or an active continental margin (Chen and Jahn, 2004)? and (2) whether the northern margin of East Junggar was formed by the northward subduction of the Junggar Ocean (Wan et al., 2011; Zhang et al., 2009) or the southward subduction of Kuerti-Erqis Ocean, a branch of the Paleo-Asian Ocean (Long et al., 2012; Xu et al., 2001, 2013)? Hence, more work is required to clarify these controversial issues, to better understand the metallogenesis in the East Junggar and its relationship to the tectonic evolution of the Late Paleozoic.

The Laoshankou district is a significant Fe-Cu-Au district on the northern margin of East Junggar, which is hosted by volcanic rocks of the Beitashan Formation and extensive Late Paleozoic intrusive rocks. Previous work showed that mineralization of the Laoshankou deposit has a close temporal relationship with these igneous rocks (Li et al., 2015). Investigation of these igneous rocks can help unravel the tectonic setting of the Laoshankou deposit and also reconstruct the tectonic evolution of the northern margin of East Junggar. More importantly, it will establish the relationship between the Fe-Cu-Au mineralization and the tectonic environment in the East Junggar in the Late Paleozoic.

We present new zircon U–Pb ages, Lu-Hf isotopes, whole-rock major and trace elements and the Sr-Nd-Pb isotopic data for the volcanic and intrusive rocks of the Laoshankou deposit in order to investigate the emplacement ages, tectonic environment, petrogenesis and magmatic evolution of these rocks. These data also provide constraints on the relationship between the Fe-Cu-Au mineralization and the geodynamic setting of the Late Paleozoic East Junggar.

2. Regional geology

The East Junggar terrane is located between the Chinese Altay arc and the Harlik arc and separated by the Erqis Fault to the north and the Kelameili fault to the south (Fig. 1b). The East Junggar comprises Devonian to Permian volcanic rocks and abundant igneous intrusions, including intermediate-mafic lavas and tuffs, minor sandstones, limestone lenses, cherts and conglomerates. It is composed of the Dulate arc in the north and the Yemaquan arc in the south separated by the Armantai fault (Fig. 1b).

The northern margin of East Junggar terrane is located within the Late Paleozoic Dulate island arc, separated from the southern Altay to the north by the Erqis Fault (or Irtysh Fault). The Erqis Fault zone is over 650 km long and up to 50 km wide making it one of the largest transcurrent faults in the CAOB and consists of high-grade metamorphic rocks, abundant two-mica-garnet granites and rare pre-Devonian A-type granites (Bai, 1996).

To the south of the Erqis Fault, the northern margin of East Junggar terrane comprises dominantly Late Paleozoic volcano-sedimentary rocks and intrusions (Fig. 1c). The Late Paleozoic volcanic sequence consists of, from the bottom to top, marine pyroclastic and sedimentary rocks of the Lower Devonian Tuoranggekuduke Formation; mafic to intermediate volcanic, pyroclastic and carbonate rocks of the Middle Devonian Beitashan Formation; shallow marine fine-grained clastic rocks intercalated with intermediate and mafic volcanic rocks of the Middle Devonian Yundukala Formation; pyroclastic rocks (dominantly tuffs), interbedded sandstones, basaltic andesites, andesites and dacites of the Late Devonian Jiangzierkuduke Formation; volcano-sedimentary rocks of the Early Carboniferous Nanmingshui Formation; basalts and basaltic andesites with minor interbedded andesites, rhyolites, tuffs, siltstones and carbonaceous shales of the Late Carboniferous Batamayineishan Formation and Permian continental coal-bearing sedimentary rocks (Li et al., 2015; Zhang et al., 2009).

Abundant igneous intrusions are exposed in the northern margin of East Junggar terrane, consisting dominantly of felsic rocks, with rare intermediate-mafic rocks (Li and Chen, 2004). The tectonic evolution of the East Junggar area can be divided into three stages: island arc, collisional and post-collisional (Lu et al., 2013; Xu et al., 2001). Previous studies have shown two peaks of Paleozoic magmatism at 390–370 Ma and 320–270 Ma in the East Junggar (Lu et al., 2012; Xue et al., 2010). The older pulse is likely related to the subduction of the Junggar oceanic crust under the Yemaquan arc, whereas the younger pulse is thought to be related to collisional and post-collisional events (Lu et al., 2012; Xue et al., 2010).

3. Deposit geology

The Laoshankou district is situated 41 km to the southwest of Qinghe City at the intersection between the Erqis and Fuyun faults (Fig. 1c). The deposit is hosted by the Lower Devonian Tuoranggekuduke Formation and the Middle Devonian Beitashan Formation. The Tuoranggekuduke Formation, located northeast of the F1 fault, consists of a succession of shallow coastal facies continental clastic rocks intercalated with flysch and intermediate-mafic pyroclastic rocks or lavas, and is in unconformable faulted contact with the overlying Beitashan Formation (Fig. 2b). The Beitashan Formation is well exposed in the Laoshankou district where it generally hosts the ore bodies and is composed of intermediate-mafic volcanic rocks including picrites, basalts, basaltic andesites, andesites, basaltic and andesitic breccias, limestones and siltstones in the lower part of the formation, whereas the middle part consists of siltstones, tuffs, siliceous rocks and pebbly sandstones, and the upper part comprises rare siliceous rocks.

There are two large NW-striking faults in the area, the Fuyun Fault (F_1) in the north and the Shanqian Fault (F_2) in the south, both associated with W-striking and N-striking branching faults (Fig. 2a). In the region, the location of volcanic edifices and magmatism appears to have been controlled by the NW-striking faults. The Fuyun Fault strikes from 310° to 340° with dips of 60°–70°, whereas the Shanqian Fault has dips of ~70° with similar strikes. These W-striking and N-striking secondary faults occur between the two main faults and separate the ore district into a number of distinct sectors. Two secondary faults, the W-striking F_5 and the N-striking F_6, occur within the Laoshankou Fe-Cu-Au deposit, and have controlled the spatial distribution of the magmatism and mineralization.

The intrusive rocks in the deposit are mainly intermediate to mafic, and include biotite diorites and quartz syenites that occur along the secondary faults, F_5 and F_6. The biotite diorites crop out as dykes, apophyses

Fig. 1. (a) Simplified tectonic divisions of the Central Asian Orogenic Belt (CAOB) (modified from Chen and Jahn, 2004; Jahn et al., 2000). (b) Simplified geological map of the Chinese Altay and the East Junggar (modified from Wan et al., 2011; Windley et al., 2002). (c) Regional geological and metallogenic map of the southeastern Altay orogenic belt and northeastern Junggar terrane, northern Xinjiang (modified from Li et al., 2015; Liu et al., 2013; Zhang et al., 2009). Abbreviations: E. Euro Craton, East European Craton; NE China, Northeast China; H, Hongshanzui Fault; Ab, Abagong Fault; T, Tesibahan Fault; E, Erqis Fault; F, Fuyun Fault; A, Armantai Fault; K, Kelameili Fault; NT, Norte Terrane; CA, Central Altay Terrane; QAT, Qiongkuer-Abagong Terrane; ET, Erqis Terrane; L, Laoshankou deposit.

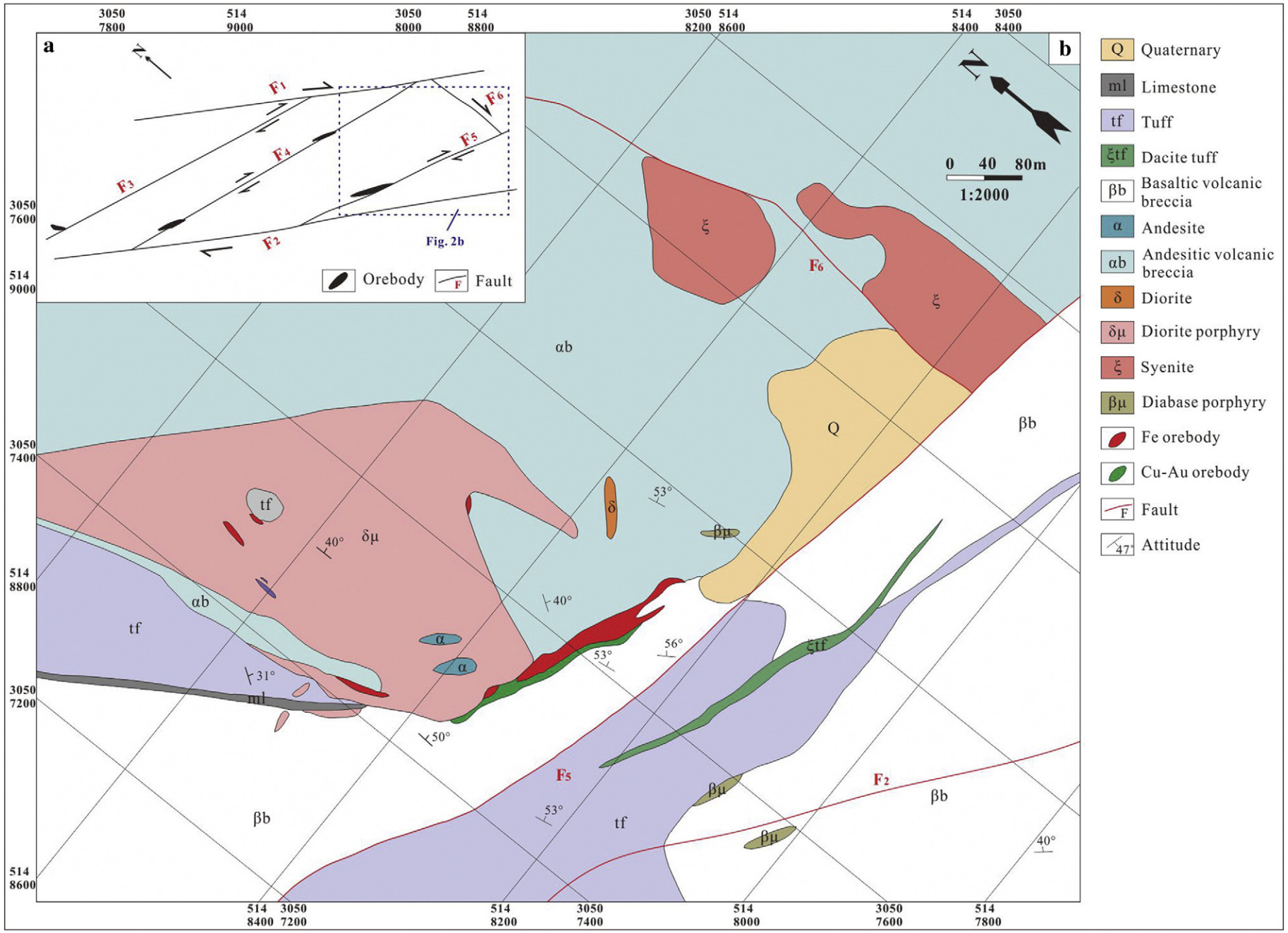

Fig. 2. (a) Simplified lineament map of the Laoshankou Fe-Cu-Au deposit. (b) Geological map of the Laoshankou Fe-Cu-Au deposit (modified from a Geological Map produced by the Geophysical Prospecting Party, Geological Survey Bureau of Xinjiang, 2005). Abbreviations: F1, Fuyun Fault; F2, Shanqian Fault; F3, F4, F5, unnamed secondary faults.

and stocks (plutons), with a total outcrop area of 2.6 km^2. They cut across the Beitashan Formation and are generally crosscut by the quartz syenites with clear contact relationship. The quartz syenites occur as dykes and apophyses, with an outcrop area of 0.8 km^2.

4. Samples and analytical methods

Based on field and petrographic observations, eleven least altered samples from the Laoshankou district, including two basalts, two andesites, one basaltic-andesitic tuff, two biotite diorites and four quartz syenites, were selected for whole-rock major and trace element geochemistry, zircon U–Pb dating and Sr-Nd-Pb-Hf isotope analysis (Table A.1).

4.1. Whole-rock major and trace element analysis

Eleven whole-rock samples were crushed to about 200 mesh in an agate mill. Whole-rock major and trace element analyses were determined at ALS Chemex (Guangzhou) Co., Ltd., China. Major element compositions were measured by wavelength dispersive X-ray fluorescence spectrometry (XRF) on fused glass disks after 0.2 g samples of rock powder were fused with 1.5 g $LiBO_2$. Major element compositions have analytical uncertainties of <5%. The loss on ignition (LOI) was determined after heating the samples to 1000 °C for three hours. For trace element analyses, about 50 mg of whole-rock powder was dissolved in capped Savillex Teflon beakers using four acid digestion and then analysed by inductively coupled plasma mass spectrometry (ICP-MS). Precision for all trace elements is estimated to be 5%.

4.2. Sr-Nd-Pb isotopic analysis

Six samples were selected for radiogenic isotope analysis. Sr-Nd-Pb isotopic compositions were measured on a Micromass IsoProbe Multi-Collector ICP-MS at the State Key Laboratory of Isotope Geochemistry, Guangzhou Institute of Geochemistry, Chinese Academy of Sciences. For Sr-Nd isotopic analysis approximately 50 mg of whole-rock powder was dissolved in distilled HF-HNO_3 at 150 °C for five days. After complete dissolution, the samples were dried and dissolved in 2.5 N HCl. Strontium and neodymium was extracted by conventional ion exchange chromatographic techniques. The measured Sr and Nd isotopic ratios were normalized to $^{86}Sr/^{88}Sr = 0.1194$ and $^{146}Nd/^{144}Nd = 0.7219$, respectively. The reproducibility of $^{87}Sr/^{86}Sr$ and $^{143}Nd/^{144}Nd$ during measurement was monitored by analysis of the standards NBS987 for Sr and Shin Etou for Nd yielding average values of 0.710243 ± 14 (2σ) and 0.512124 ± 11 (2σ), respectively. Total procedural blanks were 0.5 ng and 0.3 ng for Sr and Nd. Separation and purification of Pb was carried out on Teflon columns with a 100 μL (separation) and 40 μL bed (cleaning) of Bio-Rad AG1-X8 (100 to 200 mesh) anion exchange resin using HBr-HCl ion exchange. Lead was loaded with a Si gel onto a pre-conditioned Re filament and measured in single filament mode. A factor of 1‰ per atomic mass unit was applied for correction of instrumental mass bias using NBS SRM 981 as a reference material. Total procedural blanks for Pb were between 20 and 40 pg. Sample reproducibility is estimated at ±0.02, ± 0.015, and ±0.03 (2σ) for $^{206}Pb/^{204}Pb$, $^{207}Pb/^{204}Pb$, and $^{208}Pb/^{204}Pb$ ratios, respectively. Details of the analytical techniques are described by Liang et al. (2003).

4.3. Zircon U–Pb geochronology

Quartz syenite (TS-002) and biotite diorite (TS-003) samples were collected from the Laoshankou district for LA-ICP-MS zircon U–Pb and Hf analysis. Prior to analysis, zircons were separated through conventional magnetic and density separation techniques before hand-picking under a binocular microscope. Selected zircon grains were enclosed in epoxy resin and polished to expose the center of individual crystals. Cathodoluminescence (CL) images were used to observe the morphology and internal structures of the polished zircon grains.

U–Pb dating and in-situ trace element analyses of all zircon grains was performed using an Agilent 7500a ICP-MS coupled with a Resonetics RESOlution M-50 (193 nm ArF excimer) laser ablation system (LA) at the State Key Laboratory of Isotope Geochemistry, Guangzhou Institute of Geochemistry, Chinese Academy of Sciences. Laser ablation was conducted at a constant energy of 81 mJ/cm^{-2} with a repetition rate of 10 Hz and a spot diameter of 31 μm. The ablated material was carried by He-Ar gas to the ICP-MS via a Squid system to homogenize the signal. Each analysis incorporated a background acquisition time of approximately 20–30 s (gas blank) followed by 50 s of data acquisition during ablation of the samples. The detailed analytical procedures followed those described by Liu et al. (2010). Off-line selection and integration of background and analyzed signals, and time-drift correction and quantitative calibration for trace element analyses and U–Pb dating were performed using an in-house program ICPMSDataCal 8.3 (Liu et al., 2010). The zircon standard Temora (417 Ma; Black et al., 2003) was used for an external calibration and a Qinghu standard was used for an internal calibration during U–Pb dating. The absolute abundances of U, Th and rare earth elements were determined using an external standard glass NIST SRM 610, and ^{29}Si was used as the internal standard. Common Pb correction and age of the sample was calculated using ComPbCorr#3_17 (Andersen, 2002). Concordia diagrams and weighted mean calculations were derived using Isoplot/Ex_ver3.0 (Ludwig, 2003). Concordances are listed in Table A.4 and the weighted mean ages are quoted at the 95% confidence level.

4.4. Zircon Lu-Hf isotope analysis

The in-situ Hf isotope analyses were performed using a Neptune Plus MC-ICP-MS (Thermo Fisher Scientific, Germany) in combination with a Resonetics RESOlution M-50 (193 nm ArF excimer) laser ablation system (LA) at the State Key Laboratory of Isotope Geochemistry, Guangzhou Institute of Geochemistry, Chinese Academy of Sciences. The analyses for zircons were conducted using a single-spot ablation mode, and beam diameter of 44 μm, 10 Hz repetition rate and energy of 100 mJ/cm^{-2}. Helium was used as the carrier gas in the ablation cell and was merged with Argon (makeup gas) downstream of the ablation cell. In order to evaluate the reliability of the analytical data, the zircon standard Penglai was used for external standardization, and yielded a weighted mean $^{176}Hf/^{177}Hf$ ratio of 0.082906 ± 50 (σ). Each measurement consisted of 20 s of acquisition of the background signal followed by 50 s of ablation signal acquisition. Data were normalized to $^{179}Hf/^{177}Hf = 0.7325$, using exponential correction for mass bias (Segal et al., 2003). The ^{176}Lu decay constant of 1.865×10^{-11} yr^{-1} (Scherer et al., 2001) was used to calculate initial $^{176}Hf/^{177}Hf$ ratios. The chondritic values of $^{176}Hf/^{177}Hf = 0.0332$ and $^{176}Lu/^{177}Hf = 0.282772$ reported by Blichert-Toft and Albarède (1997) were used for the calculation of $\varepsilon_{Hf}(t)$ values. The depleted mantle Hf model ages (T_{DM}) were calculated using the measured $^{176}Lu/^{177}Hf$ ratios of zircon based on the assumption that the depleted mantle reservoir has a linear isotopic growth from $^{176}Hf/^{177}Hf = 0.279718$ at 4.55 Ga to 0.283250 at present, with $^{176}Lu/^{177}Hf = 0.0384$ (Griffin et al., 2000). However, this T_{DM} model age can only give a minimum age for the source material of the magma from which the zircon crystallized because fractionation between Lu and Hf occurs when zircons form. In order to circumvent such a problem, the Hf model age T_{DM}^{C} was calculated, which is derived from projecting the initial $^{176}Hf/^{177}Hf$ of a zircon (after determination of its U/Pb age) back to the depleted mantle model growth line by using a $^{176}Lu/^{177}Hf$ ratio of 0.008, the mean value for upper continental crust (Rudnick and Gao, 2003).

5. Results

5.1. Petrography

The basalts are green to grey in color with porphyritic textures and variable amounts of phenocrysts (50%–60%) of pyroxene, plagioclase, hornblende and rare titanite in a matrix of plagioclase, pyroxene and irregular granular magnetite (Fig. 3a, b). In the trachybasalt (Fig. 3b), plagioclase shows simple twinning and alteration rims of melanocratic clay minerals. Amygdaloidal chlorite, epidote and calcite occur sporadically in the basalts. Calcite occasionally occurs as veinlets.

The andesites are red-grey in color and porphyritic, with phenocrysts (50%–55%) of Na-rich plagioclase showing simple and polysynthetic twinning and alteration rims of melanocratic clay minerals, hornblende and pyroxene in a fine-grained matrix of plagioclase and minor magnetite (Fig. 3c). Accessory minerals include apatite and titanite.

Pyroclastic rocks, including tuffs, are a major part of the Beitashan Formation. The tuffs are dark gray in color and consist of ~15% basaltic and andesitic detritus, 25%–40% crystal fragments, and volcanic ash (~50%; Fig. 3d). The crystal fragments have a mineral assemblage of plagioclase (simple and polysynthetic twinning), alkali-feldspar, hornblende, with rare quartz and apatite.

The quartz syenite is pink with coarse, granular textures and massive structures (Fig. 3e). They are mainly composed of K-feldspar (carlsbad, gridiron and simple twinning), Na-rich plagioclase (simple and polysynthetic twinning), hornblende, biotite and quartz. Accessory minerals include zircon, apatite and titanite. Plagioclase, quartz mineral inclusions are poikilitically enclosed by the K-feldspar (Fig. 3e).

The biotite diorite is generally green-grey in color, with medium- to coarse-grained granular textures and massive structures. They comprise Ca-rich plagioclase, Na-rich plagioclase, K-feldspar, hornblende and biotite (Fig. 3f). Accessory minerals include zircon, apatite and titanite. Plagioclase laths show simple or polysynthetic twinning and are typically zoned. Biotite shows a banded structure and is cut by plagioclase. Plagioclase, hornblende and biotite mineral inclusions are commonly embedded in K-feldspar.

5.2. Whole-rock geochemistry

Whole-rock major, trace, and REE element composition of representative samples from the Laoshankou district are presented in Tables A.2 and A.3.

5.2.1. Volcanic rocks

Basaltic rocks of the Laoshankou district show a limited range of SiO_2 from 47.55 to 52.97 wt.% and a wide range of Al_2O_3 from 8.44 to 18.21 wt.%. Their A/CNK ratios mostly range from 0.38 to 0.77 and A/NK values show a range of 1.20 to 2.22, consistent with metaluminous compositions. The sum of K_2O and Na_2O varies from 2.99 to 7.24 wt.% with Na_2O/K_2O ratios ranging from 0.7 to 30, reflecting the large variation in Na_2O from 2.40 to 6.50 wt.%. On the Nb/Y-Zr/TiO_2 diagram (Fig. 4a) the rocks mostly fall in the sub-alkaline basalt or andesite fields. They have high concentrations of FeO^T and MgO (4.62 to 11.15 wt.% and 3.26 to 15.91 wt.%, respectively), and low TiO_2 contents of 0.50 to 1.20 wt.%, following a calc-alkaline trend (Fig. 4b–d). Mg# values vary from 51 to 75.

Compared to the basaltic rocks, andesitic rocks from the Laoshankou district are characterized by higher SiO_2 contents from 55.44 to 62.10 wt.% and higher total ($Na_2O + K_2O$) from 6.36 to 9.73 wt.%, but lower Na_2O/K_2O ratios from 0.4 to 14. Moreover they have lower FeO^T (4.43 to 7.41 wt.%), much lower TiO_2 and MgO contents (0.41 to 0.84 wt.% and 2.11 to 2.77 wt.%, respectively) than the basaltic rocks. Most samples plot in the andesite or basalt fields (Fig. 4a), and follow a calc-alkaline trend on the Co/Th,

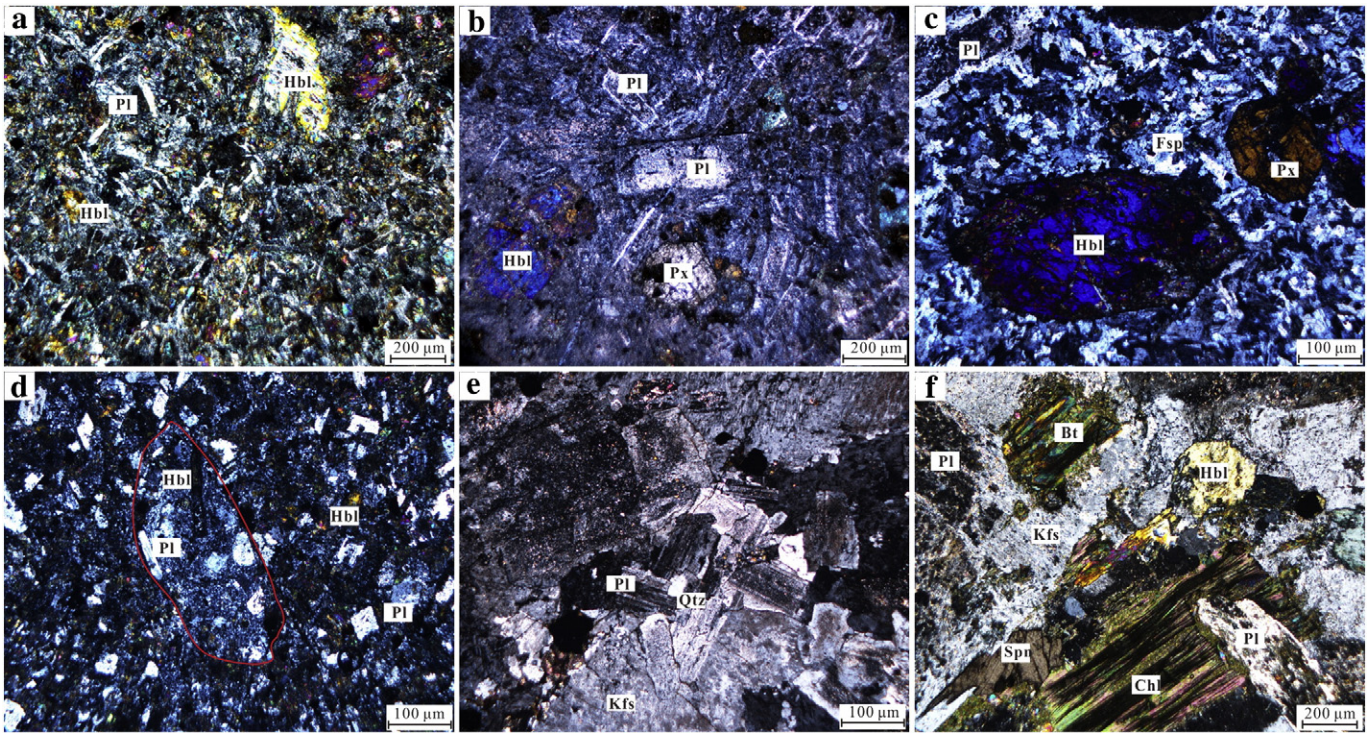

Fig. 3. Photomicrographs of the main facies types under cross-polarized light for samples from the Laoshankou district. (a) hornblende and plagioclase phenocrysts of the basalts in the Beitashan Formation (TS-006); (b) hornblende, pyroxene and plagioclase phenocrysts of the trachybasalts in the Beitashan Formation (LS-022); (c) fine-grained matrix of plagioclase with phenocrysts of amphibole, pyroxene and plagioclase in the andesites of the Beitashan Formation (LS-025); (d) andesitic detritus in the basaltic-andesitic tuff (LS-017); (e) laths of plagioclase and quartz are enclosed within K-feldspar in the quartz syenite (LS-030); (f) plagioclase, biotite, hornblende and sphene are enclosed within K-feldspar in the biotite diorite (TS-003). Hbl – hornblende; Pl – plagioclase; Px – pyroxene; Fsp – feldspar; Kfs – K-feldspar; Bt – biotite; Spn – sphene; Qtz – quartz; Chl – chlorite.

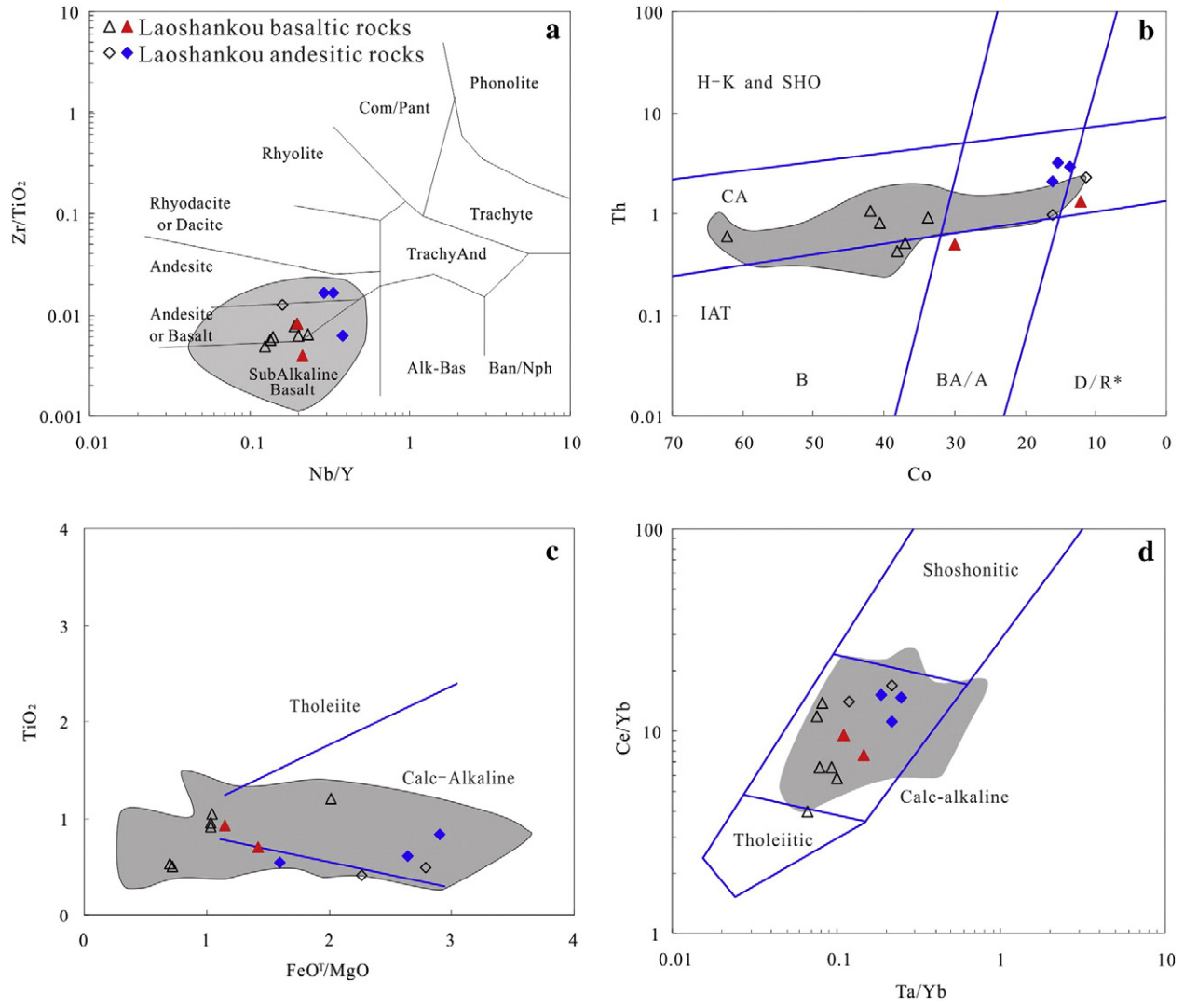

Fig. 4. (a) Nb/Y versus Zr/TiO_2*0.0001 diagram (Winchester and Floyd, 1977). (b) Co versus Th discrimination diagram (Hastie et al., 2007). (c) TiO_2 versus FeO^T/MgO diagram (Miyashiro and Shido, 1975). (d) Ta/Yb versus Ce/Yb diagram (Pearce, 1982). Com/Pant: Comendite/Pantellerite; TrachyAnd: TrachyAndesite; Ban/Nph: Basanite/Nephelinite; Alk-Bas: alkaline-basalt; IAT: island arc tholeiite; CA: calc-alkaline; H-K: high-K calc-alkaline; SHO: shoshonite; B: basalts; BA: basaltic andesites; A: andesites; D: dacites; R*: rhyolites. Field in gray represents the volcanic rocks of the Beitashan Formation. Data for volcanic rocks in the Laoshankou are from Zhang et al. (2009) and Chai et al. (2012). Data for volcanic rocks of the Beitashan Formation are from Chai et al. (2012) and Zhang et al. (2009).

Ta/Yb-Ce/Yb, FeO^T/MgO-TiO_2 diagrams (Fig. 4b–d). Mg# varies from 42 to 57, which is lower than in the basaltic rocks.

Total REE contents of the basaltic rocks vary from 34.9 to 63.2 ppm (averaging 48.9 ppm) with $(La/Yb)_N$ ratios from 1.09 to 4.26 (averaging 2.46), variable Eu anomalies (δEu = 0.72 to 1.16, averaging 0.97) and slightly positive Ce anomalies (δCe = 0.99 to 1.07, averaging 1.02; Fig. 5a, c).

Compared with the basaltic rocks, the andesitic rocks are characterized by higher ∑REE contents from 60.3 to 87.9 ppm (averaging 72.0 ppm) and higher $(La/Yb)_N$ ratios from 3.47 to 5.85 (averaging 4.73). They also display slightly depleted Eu anomalies (δEu = 0.83 to 1.06, averaging 0.94) and positive Ce anomalies (δCe = 0.99 to 1.60, averaging 1.13).

Multi-element variation diagrams of all volcanic samples are characterized by an enrichment in large-ion lithophile elements (LILEs; Ba, K and Sr) relative to high field strength elements (HFSEs; Nb, Ta, Zr, Ti, Th and Y) and heavy rare earth element (HREEs; Yb and Lu; Fig. 5b, d) with positive P anomalies.

5.2.2. Intrusive rocks

The quartz syenite is characterized by SiO_2 contents ranging from 59.94 to 63.60 wt.% and Al_2O_3 contents from 17.67 to 19.13 wt.%. All samples show elevated $K_2O + Na_2O$ contents varying from 11.65 to 13.02 wt.% and low Na_2O/K_2O varying from 0.6 to 0.9. A/NK and A/CNK range from 1.09 to 1.19 and 0.90 to 1.01, respectively, indicative of slightly metaluminous compositions. Whole rock Mg# ranges from 27 to 35. Total REE contents of the quartz syenite vary from 22.8 to 65.4 ppm (averaging 35.4 ppm) with $(La/Yb)_N$ ratios from 4.77 to 6.94, averaging 6.01. They are characterized by variable Eu anomalies (δEu = 0.79 to 1.73, averaging 1.33) and slightly depleted Ce anomalies (δCe = 0.70 to 1.03, averaging 0.85; Fig. 5e).

Biotite diorites have SiO_2 concentrations between 51.68 and 55.10 wt.%, are metaluminous with A/NK and A/CNK values ranging from 1.44 to 1.63 and 0.72 to 0.81, respectively, and have moderate Al_2O_3 (15.71–17.64 wt.%). Contents of K_2O and Na_2O (Na_2O = 2.98–3.83 wt.%; K_2O = 4.45–5.73 wt.%) are lower than quartz syenites with lower Na_2O/K_2O ratios ranging from 0.54 to 0.76. They have MgO and

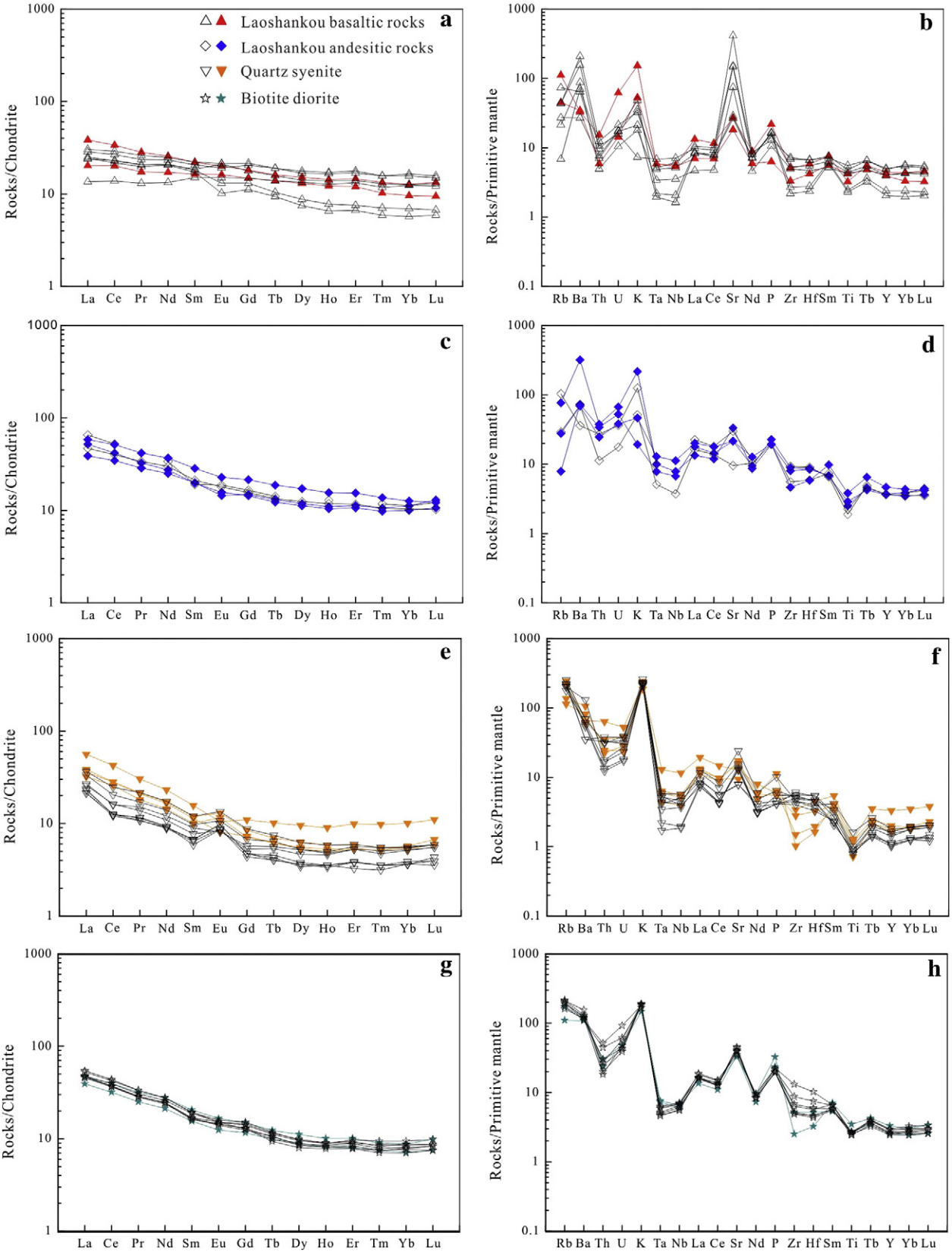

Fig. 5. Chondrite-normalized rare earth element (REE) and primitive mantle-normalized trace element spider diagrams for volcanic rocks and intrusive rocks from the Laoshankou district (normalizing values from Sun and McDonough, 1989). (a)-(b) basaltic rocks; (c)-(d) andesitic rocks; (e)-(f) quartz syenites; (g)-(h) biotite diorites. Data of volcanic rocks in the Laoshankou district are from Zhang et al. (2009) and Chai et al. (2012). Data for intrusive rocks in the Laoshankou district are from Lu et al. (2013).

Mg# ranging from 3.79 to 6.22 wt.% and 60 to 62, respectively, higher than those of quartz syenites. The biotite diorite has higher total REE contents than the quartz syenite (52.6 and 69.5 ppm, averaging 62.1 ppm) with $(La/Yb)_N$ ratios from 5.34 to 6.81, averaging 5.86. All biotite diorites display slightly depleted Eu anomalies from 0.88 to 1.02, averaging 0.95 but no Ce anomalies ($\delta Ce = 0.96$ to 1.01, averaging 0.99; Fig. 5g).

The primitive mantle-normalized multi element diagrams (Fig. 5f, h) for the intrusive rocks from the Laoshankou district are broadly similar, with enriched LILEs and P relative to HFSEs.

5.3. Zircon morphology, geochemistry and geochronology

The U–Pb data for zircon grains from samples TS-002, TS-003 in the Laoshankou district are listed in Table A.4. Typical CL images are presented in Fig. A.1, together with $^{206}Pb/^{238}U$ ages and $\varepsilon_{Hf}(t)$ values for the relevant spots.

5.3.1. Quartz syenite

These zircon grains from the quartz syenite are generally euhedral and dark to light brown in color, with grain sizes ranging from 100 to 200 μm in length. Cathodoluminescence images of zircon grains reveal generally magmatic oscillatory, banded, sector zoning (Fig. A.1), suggesting that the zircon grains are generally of magmatic origin. The chondrite-normalized REE diagrams (Fig. 6e) are also consistent with magmatic zircons as they have normalized patterns characterized by a steeply-rising slope from the LREEs to the HREEs and with pronounced positive Ce anomalies and minor depleted Eu anomalies. Uranium concentrations of zircons from sample TS-002 vary widely from 446 to 1570 ppm and Th concentrations range from 215 to 1684 ppm, with Th/U ratios of 0.33 to 1.28 consistent with a magmatic origin. $^{206}Pb/^{238}U$ ages can be divided into three groups (Fig. 6a), with weighted mean ages of 407 ± 5 Ma, 391 ± 5 Ma and 376 ± 2 Ma (MSDW = 0.13). The youngest age of 376 ± 2 Ma (MSDW = 0.13) with the most analytical spots is interpreted to be the crystallization age of the quartz syenite. The core-overgrowth structures with homogeneous cores and banded rims in the CL images (sp. 4, 8, 25; Fig. A.1) indicate that the quartz syenite magma inherited zircons from older crustal rocks or from early crystallized magmas (Belousova et al., 2002). The oldest age of 407 ± 5 Ma is interpreted to represent inherited zircons from an older magmatic event, consistent with the work of Lu et al. (2012). The 391 ± 5 Ma ages, are similar to the Beitashan Formation, and are interpreted to have been inherited from that unit or similar Middle Devonian host rocks.

5.3.2. Biotite diorite

The zircons from the biotite diorite samples have euhedral, prismatic shapes and are partly broken, ranging from light to dark brown in color under CL. They are generally 50 to 150 μm in length with magmatic oscillatory and banded zoning. Some zircon grains contain dark homogeneous cores with distinct core-rim structures (sp. 18; Fig. A.1). The chondrite-normalized REE patterns with relatively enriched HREE, positive Ce and depleted Eu (Fig. 6f) indicate a magmatic origin for all zircons from the biotite diorite. Uranium concentrations of zircons vary widely from 118 to 482 ppm, with one up to 771 ppm (sp. 18; Fig. A.1) and Th concentrations range from 46.3 to 394 ppm, with one up to 809 ppm (sp. 18; Fig. A.1). Th/U ratios range from 0.38 to 1.05, with the majority greater than 0.1, consistent with a magmatic origin. The U–Pb zircon ages of sample TS-003 can be separated into three different groups (Fig. 6c). The younger group yielded $^{206}Pb/^{238}U$ ages of 379 ± 2 Ma (MSDW = 0.80), which is likely the emplacement age for the biotite diorite (Fig. 6d). The older zircons have $^{206}Pb/^{238}U$ ages from 407 ± 6 Ma to 391 ± 4 Ma, which are similar to the inherited ages of the quartz syenite, suggesting these zircon ages are inherited from older rocks, consistent with the core-overgrowth structure in the older zircons (sp.11, 18; Fig. A.1).

5.4. Zircon Hf isotopic compositions

The Hf isotopic data for zircon grains from samples TS-002 and TS-003 in the Laoshankou district are listed in Table A.5 and illustrated in Fig. 7a. Twelve in situ Hf isotope analyses were determined on zircon grains from the quartz syenite (sample TS-002). They exhibit positive $\varepsilon_{Hf}(t)$ values of 7.95 to 12.72, yielding T^{C}_{DM} model ages ranging from 868 to 561 Ma and $^{176}Hf/^{177}Hf$ ratios ranging from 0.282798 to 0.282904.

Twelve in situ Hf isotope analyses were determined on zircon grains from the biotite diorite (sample TS-003), and yielded $\varepsilon_{Hf}(t)$ values of 9.74 to 13.26, and T^{C}_{DM} model ages of 761 to 530 Ma with $^{176}Hf/^{177}Hf$ ratios ranging from 0.282817 to 0.282920.

5.5. Sr-Nd-Pb isotope compositions

The results of Sr-Nd and Pb isotope analyses are reported in Tables A.6 and A.7 and illustrated in Fig. 7b–d. Initial isotopic ratios were calculated back to the crystallization ages of intrusive rocks (this study) and the proposed age (385 Ma) of volcanic rocks (Zhang et al., 2009).

Volcanic rocks for Laoshankou yielded initial $^{87}Sr/^{86}Sr$ ratios of 0.7042–0.7044, $\varepsilon_{Nd}(t)$ values of 5.5–5.6 and two-stage depleted mantle Nd model ages (T_{2DM}) of 685–681 Ma. Calculated initial Pb isotope ratios of $(^{206}Pb/^{204}Pb)_{t,}$ $(^{207}Pb/^{204}Pb)_t$ and $(^{208}Pb/^{204}Pb)_t$ are 17.87–17.95, 15.456–15.460, and 37.58–37.62, respectively.

Quartz syenites for Laoshankou yielded initial $^{87}Sr/^{86}Sr$ ratios of 0.7046–0.7053, $\varepsilon_{Nd}(t)$ values of 5.6–6.3 and two-stage depleted mantle Nd model ages (T_{2DM}) of 673–609 Ma. The $(^{206}Pb/^{204}Pb)_t$, $(^{207}Pb/^{204}Pb)_t$ and $(^{208}Pb/^{204}Pb)_t$ ratios range from 17.98–18.00, 15.458–15.462 and 37.55–37.56, respectively.

Biotite diorites in Laoshankou yielded initial $^{87}Sr/^{86}Sr$ ratios of 0.7041–0.7049, $\varepsilon_{Nd}(t)$ values of 5.2–6.5 and two-stage depleted mantle Nd model ages (T_{2DM}) of 704–603 Ma, with similar $(^{206}Pb/^{204}Pb)_t$ (17.94–18.02), $(^{207}Pb/^{204}Pb)_t$ (15.452–15.462), $(^{208}Pb/^{204}Pb)_t$ (37.59–37.61) ratios to the quartz syenite.

6. Discussion

6.1. Timing of magmatism and mineralization

The abundant crinoid stems, coral, shellfish and radiolarian fossils in the outcrops of the Laoshankou district have been used to place the Beitashan Formation into the Middle Devonian (Chai et al., 2012). This is consistent with a zircon U–Pb age of 381 ± 2 Ma (MSWD = 1.4) reported for a basalt in the Laoshankou district by Chai et al. (2012). The new ages of 376 ± 2 Ma and 379 ± 2 Ma ages from this study most likely represent the emplacement ages of the quartz syenite and biotite diorite, respectively and are consistent with previous work in the Laoshankou Fe-Cu-Au deposit, including zircon U–Pb ages of 379.3 ± 2.3 Ma and 379.7 ± 3 Ma for the biotite diorite and the diorite porphyry (Lu et al., 2012). Regional geochronological data for intrusive rocks in ore deposits along the northern margin of East Junggar is compiled in Table A.8 and is broadly comparable to the data generated in this study. The combined results suggest a voluminous early Late Paleozoic magmatic event (390–370 Ma) in the northern margin of East Junggar (Lu et al., 2012; Xue et al., 2010).

Yang et al. (2012a) proposed that the Late Devonian Kalaxianger porphyry Cu metallogenic belt formed in an oceanic island arc at the northern margin of East Junggar between 378 to 374 Ma, coeval with the Late Paleozoic magmatic event. Geochronological data for the deposits includes a Re-Os isochron age of 376.9 ± 2.2 Ma for molybdenite in the Halasu porphyry copper ore district (Wu et al., 2008) and Re-Os ages of 378.3 ± 5.6 Ma and 373.9 ± 2.2 Ma for molybdenite in the Halasu and Yulekenhalasu porphyry copper deposits, respectively (Yang et al., 2012b). For the Laoshankou Fe-Cu-Au deposit, Li et al. (2015) has reported a molybdenite Re-Os age of 383.2 ± 4.5 Ma. These previous Re-Os ages for molybdenite are consistent with the zircon LA-ICP-MS U–Pb ages of the mineralization-related Beitashan basalts (381 ± 2 Ma; Chai et al., 2012), diorite porphyry (379.7 ± 3.0 Ma; Lu et al., 2012), quartz syenite (376 ± 2 Ma, this study) and biotite diorite (379 ± 2 Ma, this study) in the Laoshankou district. This indicates a possible Late Devonian Fe-Cu-Au metallogenic event

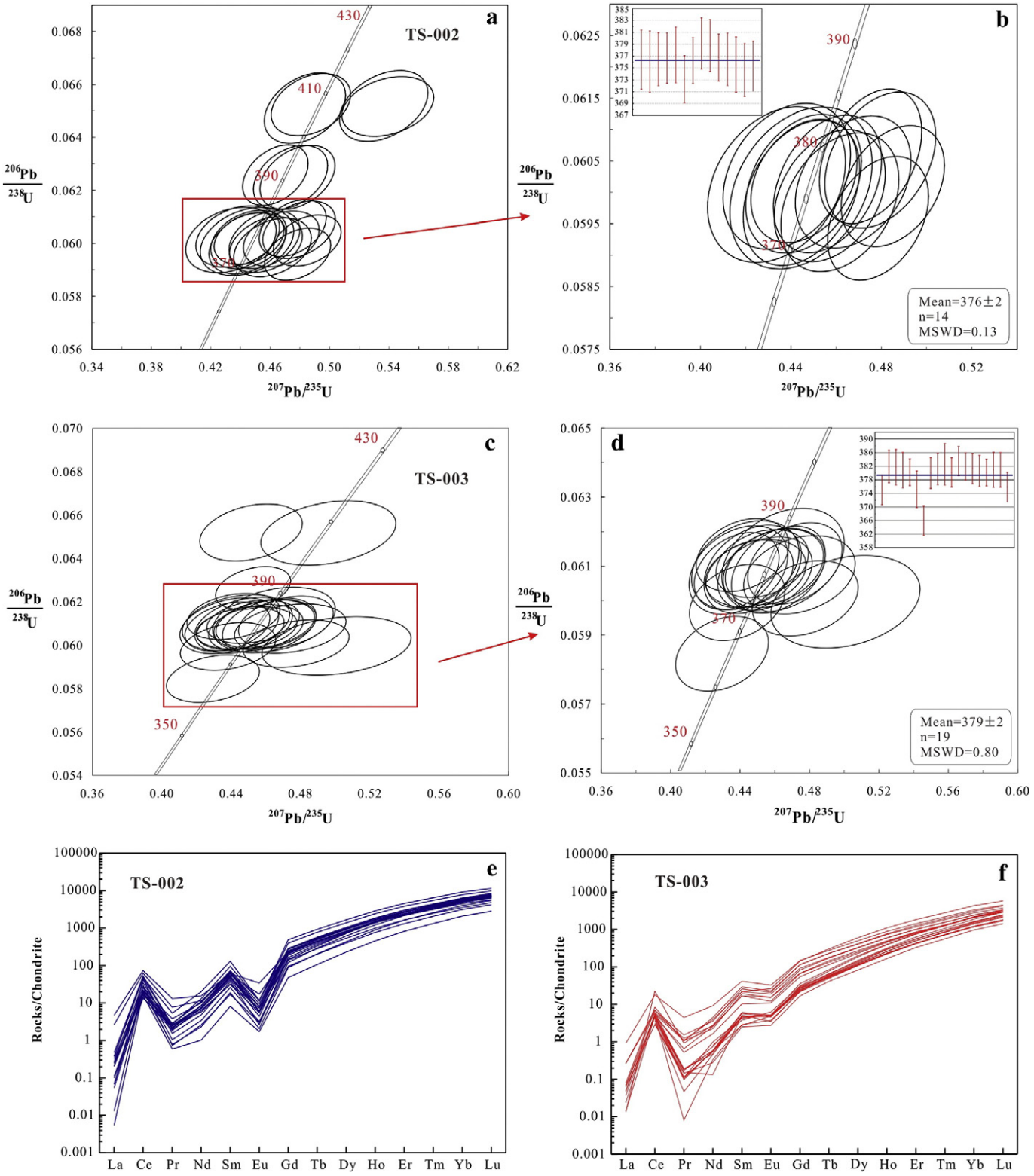

Fig. 6. (a)-(d) LA-ICP-MS zircon U–Pb concordia diagrams and $^{206}Pb/^{238}U$ average ages for the quartz syenite (a, b) and the biotite diorite (c, d) from the Laoshankou district. (e)-(f) Chondrite-normalized rare earth element (REE) of zircon grains for quartz syenite (e) and the biotite diorite (f) from the Laoshankou district. The group plotted in (b) and (d) represent the emplacement ages of the quartz syenite has been underlined by red square in (a) and (c).

on the northern margin of East Junggar, which formed in an oceanic island arc environment coevally with the porphyry Cu mineralization. The coexistence of contemporaneous Fe-Cu-Au and porphyry Cu deposits has also been identified in the Mesozoic Central Andes, suggesting a close relationship between these styles of mineralization and arc magmas (Chen et al., 2013).

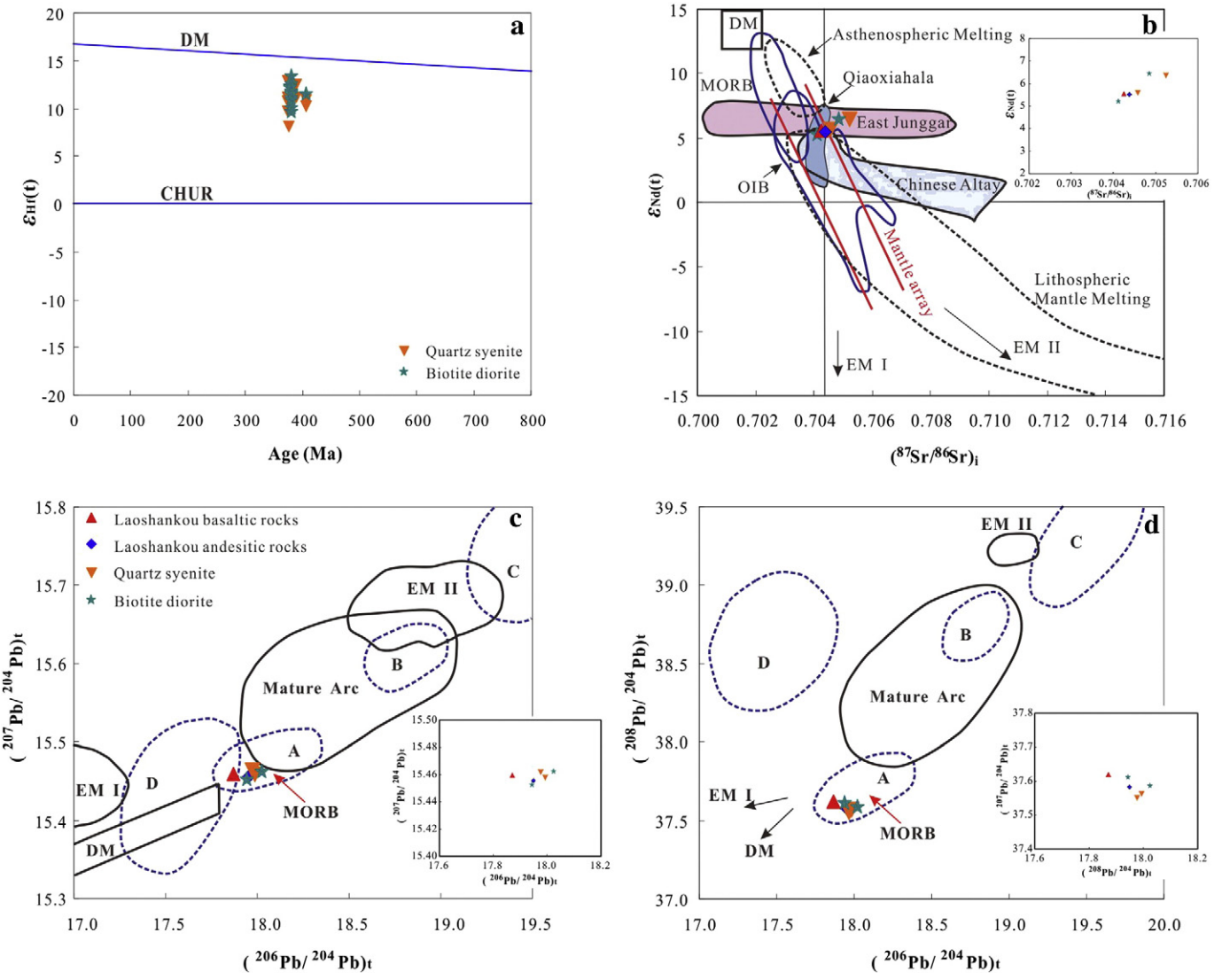

Fig. 7. (a) Diagram of $\varepsilon_{Hf}(t)$ values versus crystallizing ages for zircons of intrusive rocks. (b) $\varepsilon_{Nd}(t)$ vs $(^{87}Sr/^{86}Sr)_i$ diagram (White and Hofmann, 1982; Zindler and Hart, 1986) for volcanic and intrusive rocks. Fields for asthenospheric and lithospheric mantle melting from Wilson (1989) and Davies and von Blanckenburg (1995); fields for MORB, OIB, EM I and EM II from Zindler and Hart (1986); the data for Qiaoxiahala from Wan and Zhang (2006); the data for the East Junggar from Chen and Jahn (2004), Han et al. (1997), the data for Chinese Altai from Wang et al. (2009); mantle array from Arculus and Powell (1986) and Wilson (1989). (c)-(d) plots of $(^{206}Pb/^{204}Pb)_t$ vs. $(^{207}Pb/^{204}Pb)_t$ and $(^{208}Pb/^{204}Pb)_t$ ratio diagrams (Zartman and Doe, 1981; Zindler and Hart, 1986) for volcanic and intrusive rocks. Fields for A, B, C, D, Mature Arc and MORB from Zartman and Doe (1981); Fields for DM, EM I and EM II from Zindler and Hart (1986). Abbreviations: DM: depleted mantle; CHUR: chondritic uniform reservoir; MORB: mid-ocean-ridge basalt; OIB: ocean island basalts; EM I: enriched mantle I; EM II: enriched mantle II. Dashed lines in (c) and (d) enclose probable average values (A = mantle; B = orogene; C = upper crust; and D = lower crust).

6.2. Petrogenesis

6.2.1. Petrogenesis of the volcanic rocks

The volcanic rocks of the Beitashan Formation fall in the calc-alkaline field, are comprised dominantly of basalt-andesite-dacite-rhyolite (BADR) volcanic series rocks, and are typical of subduction-related arc volcanic rocks (Fig. 4; Green and Ringwood, 1968). The majority of volcanic rocks from the Laoshankou district lie in the field of calc-alkaline island arc basalts on a range of discrimination diagrams (Fig. 11). Samples that plot outside of the island arc field (mainly andesites) are likely the result of fractional crystallization as discussed below.

We treat the most mafic basalt samples as primary magma compositions, as they have high MgO, Ni and Cr contents. Most major oxide and trace elements show well-defined positive or negative correlations with increasing SiO_2 contents (Figs. 9 and 10), likely the result of fractional crystallization of different mineral phases during the evolution from basaltic primary magma to andesites. The negative correlation between MgO, MnO, $Fe_2O_3^T$ and SiO_2 are interpreted to be the result of hornblende fractionation whereas decreasing CaO and increasing Na_2O, K_2O, Ba with increasing SiO_2 suggest that fractional crystallization was dominated by clinopyroxene and calcic plagioclase, with only a minor role for K-feldspar (Figs. 9 and 10; Kaygusuz et al., 2014; Temizel et al., 2012). Fractionation of clinopyroxene is consistent with the negative correlations between Zr/Hf ratios and Sc concentrations and positive correlations between Zr/Hf and Nb/Ta ratios, whereas fractionation of hornblende is supported by negative correlations between Zr/Hf and Nb/Ta ratios, since Nb will preferentially partition into hornblende relative to Ta. As Sc is compatible in clinopyroxene, fractionation of these minerals will result in low Sc and Nb/Ta in coexisting melts (Fig. 8c, d; Green, 1995; Tiepolo et al., 2000). The weak negative correlation between Ni and SiO_2 (Fig. 10) indicates that fractional crystallization of olivine did not play a major role during this process (Kaygusuz et al., 2014; Temizel et al., 2012). All these variations can be explained by fractionation of the common mineral phases clinopyroxene ± plagioclase ± hornblende in the andesite (Fig. 3b). Using trace elements compositions in the FC–AFC–FCA and

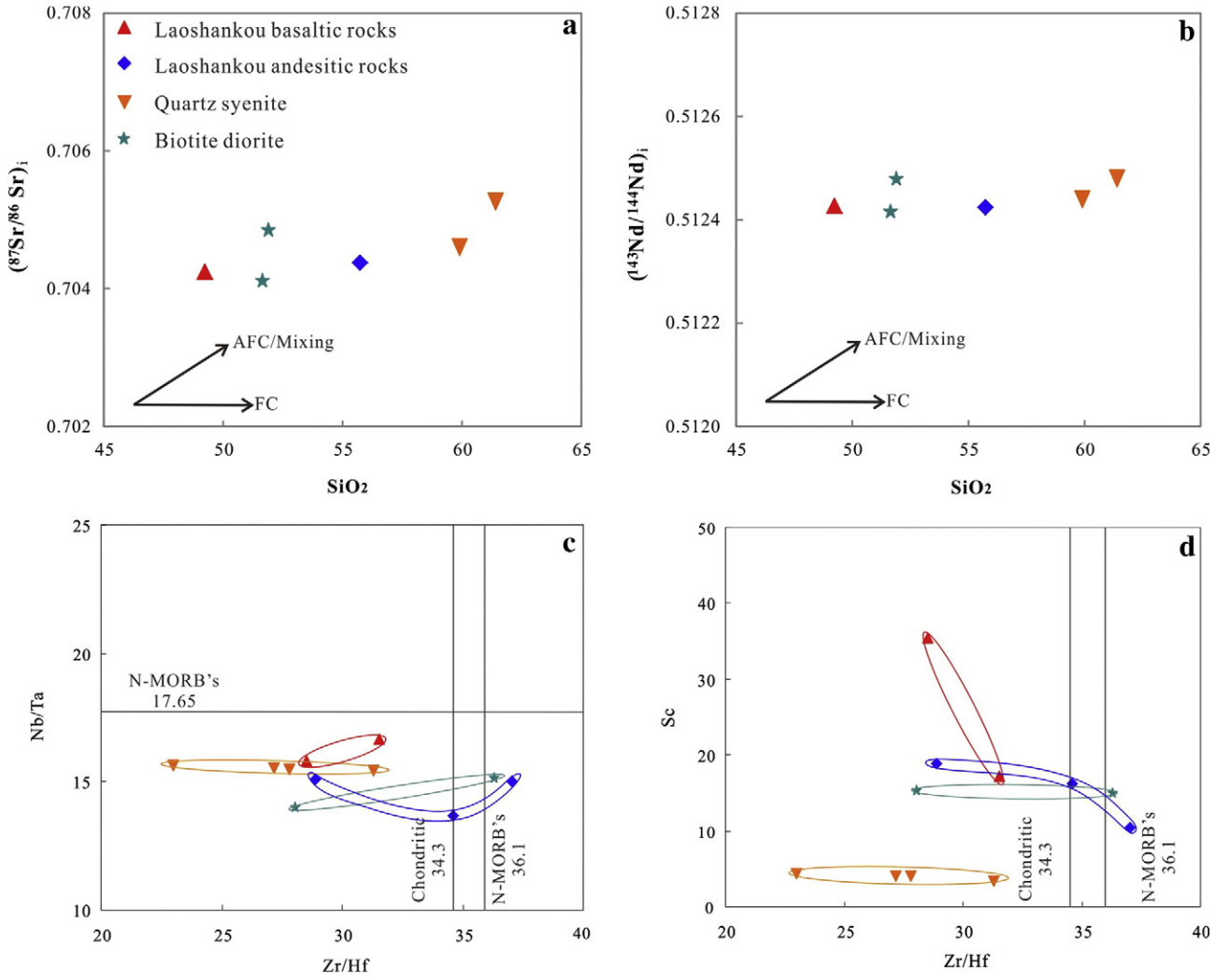

Fig. 8. Diagrams of (a) SiO_2 vs $(^{87}Sr/^{86}Sr)_i$, (b) SiO_2 vs $(^{143}Nd/^{144}Nd)_i$, (c) Zr/Hf vs. Nb/Ta and (d) Zr/Hf vs. Sc showing possible fractional crystallization (FC) and assimilation-fractional crystallization (AFC) trends for volcanic and intrusive rocks from the Laoshankou district.

mixing modeler (Ersoy and Helvacı, 2010) to model the fractional crystallization (FC) process, we estimate that 45% plagioclase, 25–30% clinopyroxene and 25–30% hornblende were fractionated from the residual magma consistent with the composition of the andesite.

The similar trends on the chondrite-normalized REE and primitive mantle-normalized multi element diagrams (Fig. 5) suggest that all the volcanic rocks were likely derived from a similar magmatic source, or even the same magma chamber. Three potential source components may have contributed to the genesis of subduction zone magmatism: (1) the mantle wedge above the subducted slab, (2) the subducted slab (melts and fluids), and (3) the arc crust (Defant and Drummond, 1990). In order to minimize the effects of fractional crystallization, we use the incompatible elements (Nb, U, Ce, Th and HREE) to assess the petrogenesis.

Experimental studies have shown that the Mg# can be used to discriminate between melts derived purely from the crust and those derived from the mantle (Rapp and Watson, 1995). Melts from basaltic lower crust are characterized by low Mg# (< 40) regardless of the degree of melting, whereas those with high Mg# (> 40) require a mantle component (Rapp and Watson, 1995). The volcanic rocks from Laoshankou have relatively high Mg# (42–75, averaging 58) indicating derivation of the melts from mantle wedge. This is consistent with the enriched LILEs and LREEs relative to HFSEs and HREEs for the volcanic rocks, which indicate subduction related metasomatism by slab derived fluids (Münker et al., 2004; Schiano et al., 1995). Moreover, elevated Ce/Th (6.6–25.5), Ba/Th (109–1460) and the absence of pronounced depleted Ce anomalies suggest that there has been no significant assimilation of subducted sediment, as this would result in elevated Th and low Ce/Th (~8), Ba/Th (~111) ratios and depleted Ce anomalies (Plank and Langmuir, 1998). The low Nb (1.16–8.00 ppm) contents of the volcanic rocks suggest the absence of melts derived from subducted oceanic crust, which can metasomatize the mantle wedge and generate Nb-enriched basaltic magmas (Hollings and Kerrich, 2000; Wyman et al., 2000). Assimilation of crustal material is an important process for modifying the trace element and isotopic composition of mantle-derived magmas (Thirlwall et al., 1994). The volcanic rocks of Laoshankou are characterized by low Th, U, Rb and Nb/U ratios, and higher Sr and Ba contents compared to continental crust (Hofmann, 1988; Rudnick and Gao, 2003), suggesting that crustal assimilation did not play a significant role in their evolution. Similarly, the positive $\varepsilon_{Nd}(t)$ values (5.5 and 5.6) and low $(^{87}Sr/^{86}Sr)_i$ ratios (0.7042 and 0.7044; Fig. 7b) overlap with the range of MORB values, consistent with a significant input of depleted mantle and precluding a crustal origin (Liu and Liu, 2014). Similarly, the weak correlations between

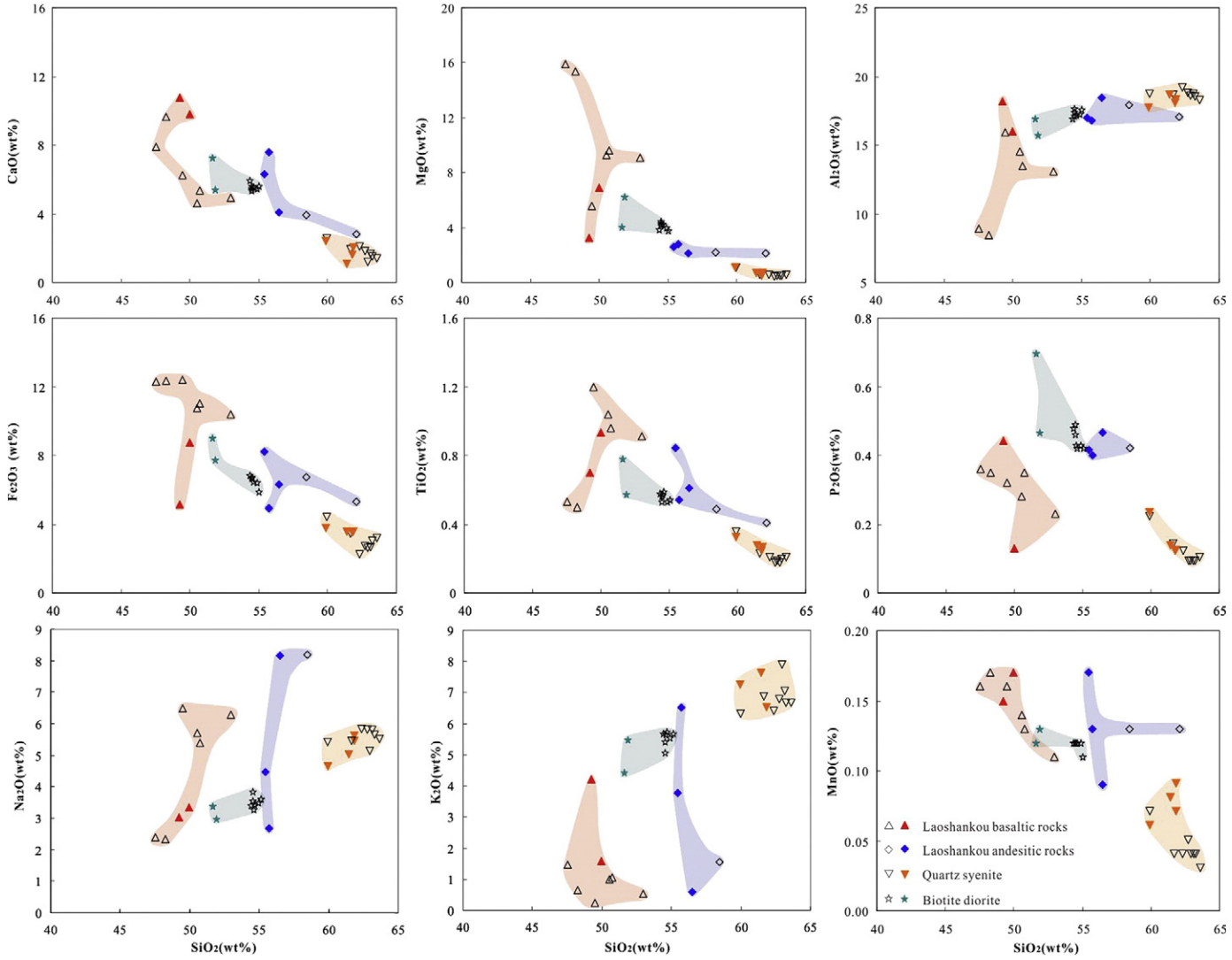

Fig. 9. Harker diagrams for CaO, MgO, Al_2O_3, $Fe_2O_3^T$, TiO_2, P_2O_5, Na_2O, K_2O and MnO versus SiO_2 for samples from the Laoshankou district. Solid area: red for basaltic rocks; blue for andesitic rocks; yellow for quartz syenite and green for biotite diorite.

$(^{87}Sr/^{86}Sr)_i$ and $(^{143}Nd/^{144}Nd)_i$ values with SiO_2 (Fig. 8) indicate that assimilation played a minor role in the generation of the volcanic rocks.

In summary, the geochemical data suggests that calc-alkaline volcanic rocks from Laoshankou were derived from a depleted mantle wedge metasomatized by slab-derived fluids, with no crustal contamination. Compositional variations within Laoshankou volcanic rocks can be explained by fractional differentiation.

6.2.2. Petrogenesis of the intrusive rocks

The intrusive rocks of the Laoshankou district are characterized by enrichment in LILEs relative to HFSEs and HREEs and marked depleted Nb, Ta and Ti anomalies with positive Sr anomalies (Fig. 5f, h), consistent with an island arc setting (Pearce and Peate, 1995). Moreover, the intrusive rocks plot within the volcanic arc granite fields on the Yb vs. Ta diagram (Fig. 11d). On the La/Yb vs. Th/Yb diagram (Fig. 11e), the samples show a trend to island arc rather than continental margin arc affinity.

Adakites are characterized by high SiO_2 (≧ 56 wt.%), Al_2O_3 (≧ 15 wt.%, rarely lower), Sr (rarely <400 ppm) and Sr/Y (> 40), and low MgO (< 3 wt.%, rarely above 6 wt.%), Y (≦ 18 ppm), HREE (Yb ≦ 1.9 ppm) and low HFSEs (Castillo, 2006). The Laoshankou quartz syenite and biotite diorite display similar geochemical characteristics with SiO_2 (59.94–63.60 wt.%; 51.68–55.10 wt.%), Al_2O_3 (17.67–19.13 wt.%; 15.71–17.64 wt.%), Sr (165–507 ppm; 685–954 ppm), Sr/Y (averaging 43, 66), MgO (0.36–1.02 wt.%; 3.79–6.22 wt.%), Y (4.57–15.0 ppm; 11.1–15.0 ppm), HREE (Yb, 0.61–1.71 ppm; 1.19–1.60 ppm) and HFSE depletions. On the Sr/Y-Y diagram, intrusions in the Laoshankou district mostly plot in the adakite field whereas volcanic rocks plot in the island arc field (Fig. 11b).

Various models have been proposed for the petrogenesis of adakites including partial melting of the subducted slab (Defant and Drummond, 1990), crustal assimilation and fractional crystallization from parental basaltic magmas (Richards and Kerrich, 2007), partial melting of thickened lower crust (Petford and Atherton, 1996) and delamination of lower crust (Kay and Kay, 1993).

The biotite diorites have relatively high Al_2O_3 (≧ 15 wt.%), MgO (3.79–6.22 wt.%), Cr (77–193 ppm), and Mg# (51–65, averaging 59) values, with no pronounced depleted Eu (0.88–1.02) anomalies and the absence of extremely high Sr/Y and La/Yb ratios characteristic of pure slab-derived melts precludes pure partial melting of thickened crust or delamination of lower crust in an intracontinental orogenic belt as a source for these rocks (Liu and Liu, 2014; Stern and Kilian, 1996). Previous studies have shown that magma derived from sources metasomatized by slab-derived fluids would have elevated Ba content

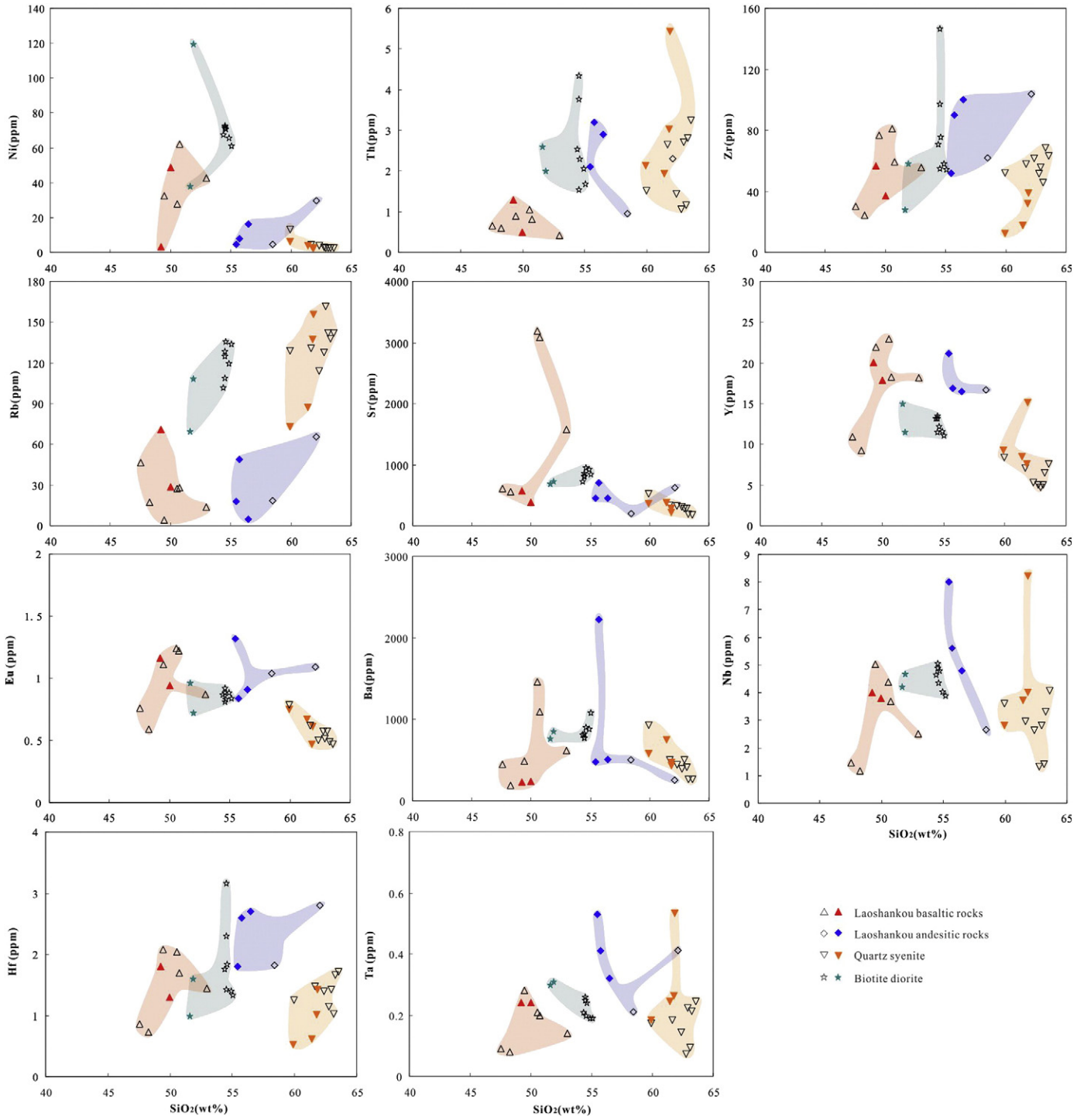

Fig. 10. Harker diagrams for Ni, Th, Zr, Rb, Sr, Y, Eu, Ba, Nb, Hf and Ta versus SiO_2 for samples from the Laoshankou district. Solid area: red for basaltic rocks; blue for andesitic rocks; yellow for quartz syenite and green for biotite diorite.

and high Ba/Th (> 170), whereas those derived from the sources modified by the subducted sediments should exhibit elevated Th contents, high Th/Yb (> 2), low Ce/Th (< 8) ratios and depleted Ce anomalies (Plank and Langmuir, 1998). The high Ba (760–1083 ppm), Ba/Th (178–645), Ce/Th (5.96–14.32, averaging 10.06) and low Th/Yb (1.19–2.73, averaging 1.81) and absence of Ce anomalies (0.96–1.01) in the intrusive rocks is consistent with the addition of the slab-derived fluids rather than subducted sediments-derived melts. The similar REE, trace element patterns and the spatial and temporal association of the intrusive rocks with the volcanic rocks of the Beitashan Formation (Fig. 7b–d) also suggests that they were derived from the same supra-subduction zone mantle wedge modified by slab-derived fluid and subsequently underwent extensive fractional crystallization.

The positive trend of SiO_2 versus $(^{87}Sr/^{86}Sr)_i$ and $(^{143}Nd/^{144}Nd)_i$ (Fig. 8a, b), and inherited zircons indicate the crustal assimilation plus fractional crystallization or mixing processes modified the intrusive magmas. This is consistent with the zoned plagioclase and mineral inclusions within K-feldspar, which have been interpreted to be the result of mixing processes (Baxter and Feely, 2002). However, positive $\varepsilon_{Hf}(t)$ values (9.74–13.26, averaging 11.55) and $\varepsilon_{Nd}(t)$ values (5.2–6.5) indicate a depleted mantle source, and suggest that assimilation of

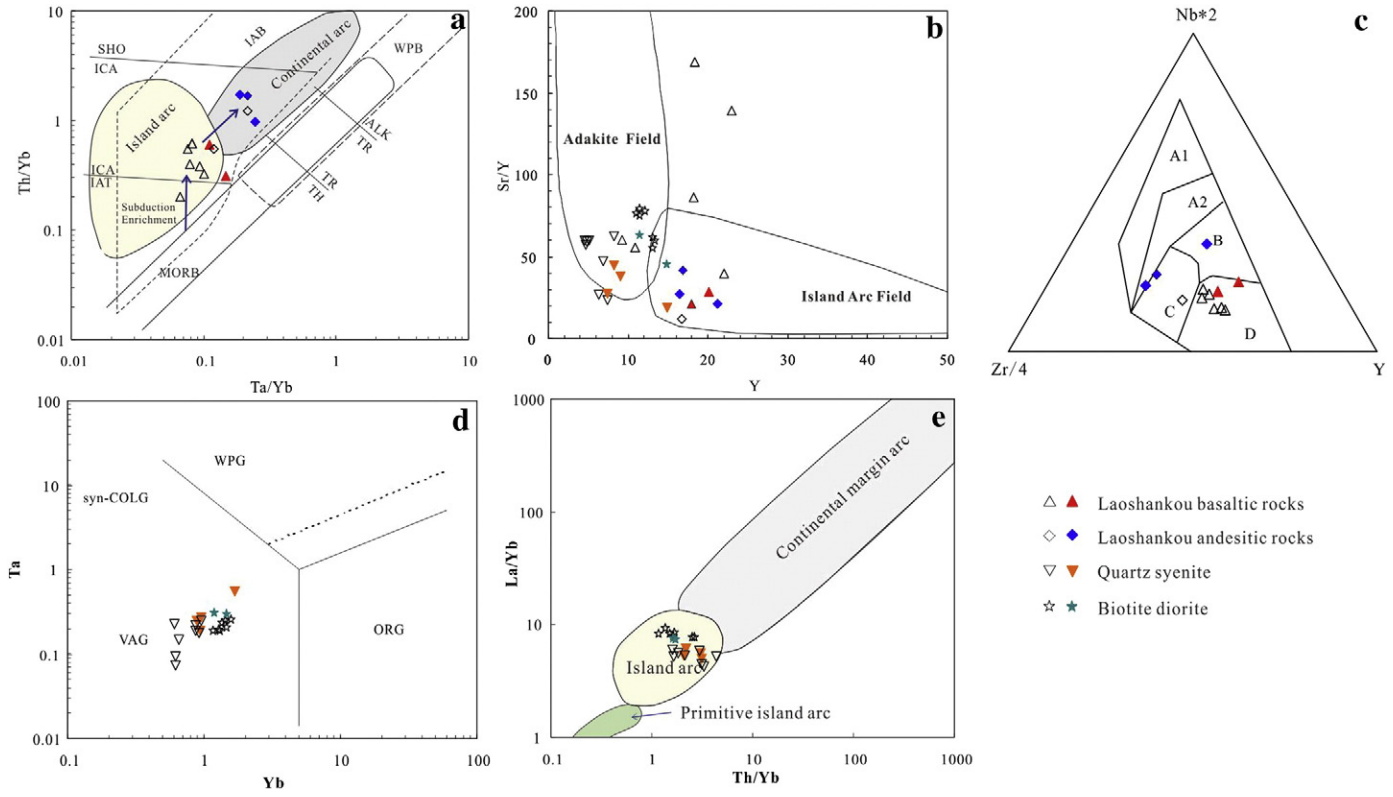

Fig. 11. (a) Th/Yb versus Ta/Yb discrimination diagram for volcanic rocks (Pearce et al., 1984). (b) Sr/Y-Y diagrams (Defant and Drummond, 1990) for the volcanic and intrusive rocks. (c) Zr/4-Y-Nb*2 discrimination diagrams for volcanic rocks (Meschede, 1986). (d) Ta vs. Yb (Pearce et al., 1984), and (e) (La/Yb) vs. (Th/Yb) (Brown et al., 1984) discrimination diagrams for intrusive rocks from the Laoshankou district. Abbreviations: IAB: island arc basalts; IAT: island arc tholeiites; ICA: island arc calc-alkaline series; SHO: shoshonitic series; WPB: within-plate basalts; MORB: mid-ocean ridge basalts; TH: tholeiites; TR: transitional basalt; ALK: alkaline basalts; A1: within-plate alkaline basalts; A2: within-plate alkaline basalts and tholeiites; B: enriched MORB; C: within-plate basalts and arc basalts; D: enriched MORB and arc basalts; C + D: arc basalts; VAG: volcanic-arc granites; Syn-COLG: syn-collisional granites; WPG: within-plate granites; ORG: ocean-ridge granites.

ancient crust was unlikely to have played a major role in the formation of the biotite diorite and that the assimilant was likely juvenile lower crust, consistent with the slightly older ages of the inherited zircons (Condie, 1989; Ketchum et al., 2013; Rapp and Watson, 1995). In summary, the biotite diorite is proposed to be the product of fractional crystallization from parental basaltic magmas, a depleted mantle wedge metasomatized by slab-derived fluids, with minor assimilation of juvenile lower crust.

The quartz syenites display trace element characteristics that are distinct from the volcanic rocks and the biotite diorite and consequently it is unlikely that they formed by fractional crystallization from the same parental basaltic magmas as the biotite diorite. The positive $\varepsilon_{Hf}(t)$ values (7.95–12.72, averaging 10.65), initial $(^{87}Sr/^{86}Sr)_i$ ratios (0.7046–0.7053), positive $\varepsilon_{Nd}(t)$ values (5.6–6.3) and Pb isotopic data are consistent with a depleted mantle wedge source (Fig. 7). However, the quartz syenite exhibits a shift to higher $(^{87}Sr/^{86}Sr)_i$ at a given $\varepsilon_{Nd}(t)$ value than the mantle array suggesting addition of a component with high $(^{87}Sr/^{86}Sr)_i$ ratios, which could be either slab-derived fluids or crustal material (Fig. 7b; Arculus and Powell, 1986). The relative enrichment of LILE to HFSE and LREE to HREE also implies a minor aqueous fluid component in the mantle source. The high Th/La (0.17–0.53), Th/Yb (1.62–4.39), low Ce/Th (2.87–10.13) ratios, low Nb and depleted Ce anomalies (0.70–1.03, averaging 0.85), indicate the addition of melts derived from subducted sediments instead of subducted oceanic crust (Hollings and Kerrich, 2000; Plank and Langmuir, 1998; Wyman et al., 2000). The low Nb/Ta (12.7–21.2, > 6.0), and high Th/U (2.57–4.91) in conjunction with the positive trend for SiO_2 versus $(^{87}Sr/^{86}Sr)_i$ and $(^{143}Nd/^{144}Nd)_i$ (Fig. 8a, b) are consistent with the crustal assimilation or mixing processes, as the ratios of Nb/Ta and Th/U for crust are 6.00 and 12.0–14.0, respectively (Rapp and Watson, 1995; Rudnick and Gao, 2003). The inherited zircons and mineral inclusions within K-feldspar are also consistent with crustal assimilation or mixing processes (Baxter and Feely, 2002). The positive $\varepsilon_{Hf}(t)$ and $\varepsilon_{Nd}(t)$ values as well as the Pb isotopic data suggest that the crustal contamination signature may be juvenile crust due to the partial melting of thicker Dulate arc crust in the Middle Devonian (Liu and Liu, 2014). In summary, quartz syenites are proposed to be the product of a depleted mantle wedge metasomatized by slab-derived fluids and subducted sediment-derived melts subsequently modified by crustal contamination.

6.3. Tectonic evolution and metallogenesis

The geodynamic evolution of the East Junggar is closely associated with the evolution of the Paleo-Asian Ocean and this collage contains two Palaeozoic arc systems: the southern Altay and the northern margin of East Junggar (Xiao et al., 2008). The current consensus is that the two arcs were created by independent subduction systems that were later amalgamated by collision (Cai et al., 2010; Long et al., 2012; Sun et al., 2008; Wan et al., 2011).

The Erqis suture zone, that separates the southern Altay and the East Junggar, includes abundant ophiolites, such as those in Kuerti, Qiaoxiahala, Buergen and Habahe, which have yielded SHRMP U–Pb ages of 352–372 Ma (Wang et al., 2011, 2012; Wu et al., 2006; H. Zhang et al., 2003). As ophiolites represent fragments of ancient oceanic crust, these ages suggest that the Kuerti-Erqis Ocean, one branch of the Paleo-Asian Ocean, still existed before 352 Ma (Early Carboniferous). As discussed above, the geochemistry of the calc-alkaline volcanic and

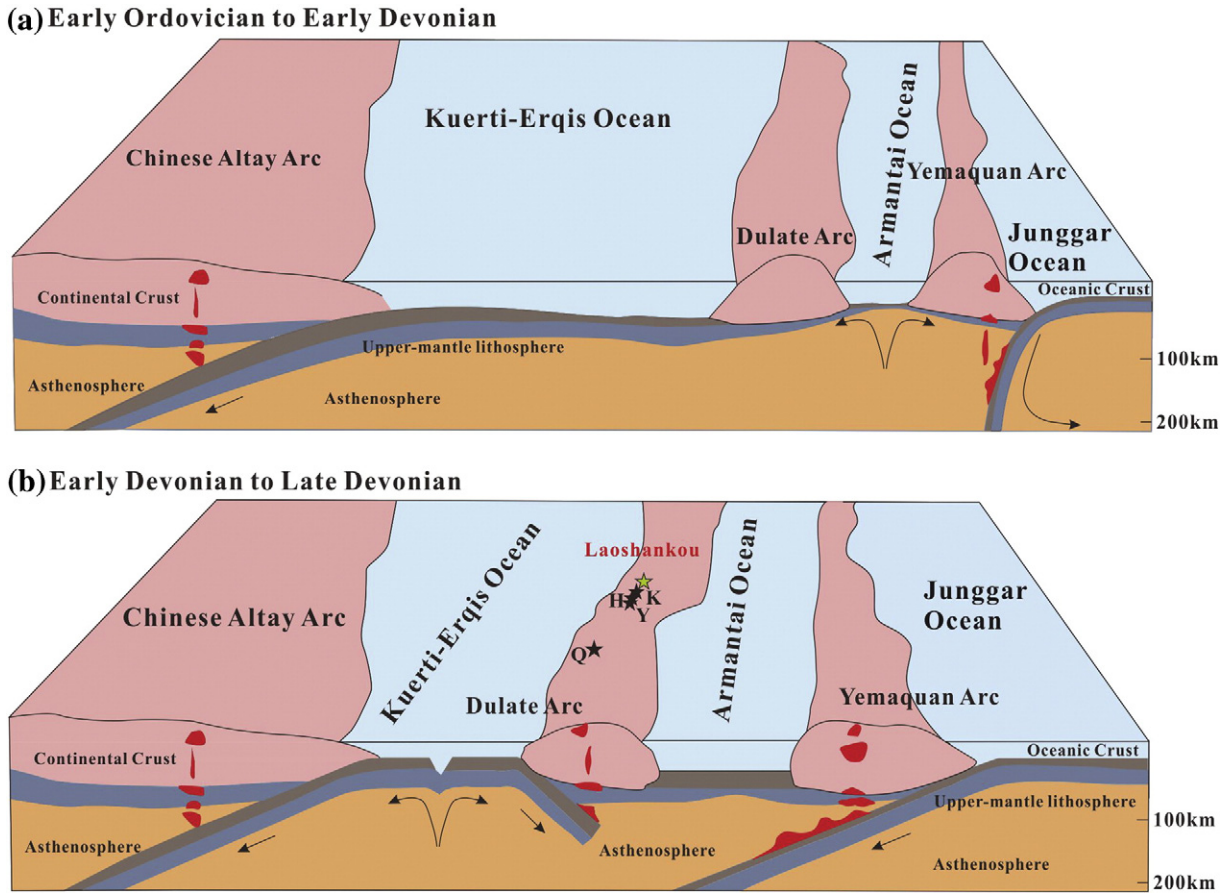

Fig. 12. The tectonic evolution of the East Junggar in the Late Paleozoic. AF: Armantai Fault; KF: Kelameili Fault; EF: Erqis Fault; H: Halasu; Y: Yulekenhalasu; K: Kalasayi; Q: Qiaoxiahala; Ka: Kalatongke; X: Xilekuduke; S: Suoerkuduke.

intrusive rocks in the Laoshankou district support a subduction-related oceanic island arc setting, rather than a continental arc origin. Combined with the precise geochronology of the volcanic and intrusive rocks of the Laoshankou district, we can conclude that from 381 to 376 Ma the northern margin of East Junggar was situated in an oceanic island arc environment. The rollback of the northward subduction zone in the Junggar Ocean (Xiao et al., 2008) and the absence of magmatism and mineralization in the Dulate arc during the Early Ordovician to Early Devonian suggests that the Dulate arc was no longer affected by the northward subduction of the Junggar Ocean after the Early Devonian (Fig. 12a). Moreover, the Lower Devonian potassic basalts and Devonian adakites, Nb-enriched basalts and boninites to the north of the Dulate arc (the northern margin of East Junggar) suggest an arc- to fore arc setting (Xu et al., 2001; Zhang et al., 2006), which implies southward subduction of the Kuerti-Erqis Ocean after the Early Devonian (Fig. 12b). The oldest inherited zircon age of ~407 Ma in the quartz syenite and biotite diorite from the Laoshankou district may constrain the initiation of the southward subduction.

The dominantly arc-related magmatism in the northern margin of East Junggar from 381 to 376 Ma is coeval with mineralization dominated by arc-related Fe-Cu-Au systems and porphyry Cu deposits. On the basis of the above considerations, the northern margin of East Junggar has the potential to host a Late Paleozoic Fe-Cu-Au metallogenic belt together with the porphyry Cu mineralization. The Fe-Cu-Au metallogenic belt in East Junggar has many features in common with the Central Andean belt, including: (1) formation in a subduction-related arc environment, (2) strong structural control on the distribution of mineralization and magmatism, and (3) mineralization hosted mainly in volcanic and volcaniclastic rocks (Sillitoe, 2003; Williams et al., 2005). Given the presence of the Late Paleozoic Heijianshan arc-related Fe-Cu-Au deposit in the East Tienshan (Zhao et al., submitted) and the Late Paleozoic Qiaoxiahala arc-related Fe-Cu-Au deposit in the East Junggar (Li et al., 2014), there is considerable potential to find several Late Paleozoic arc-related Fe-Cu-Au mineralizations in the East Junggar as well as the North Xinjiang in general.

7. Conclusions

On the basis of the petrological, geochronological and geochemical data for the Late Paleozoic volcanic and intrusive rocks from the Laoshankou district, the following conclusions can be drawn.

(1) Zircon U–Pb geochronology indicates that the volcanic rocks of the Beitashan Formation and the intrusive rocks of the Laoshankou district were emplaced from 381 Ma to 376 Ma.
(2) Sr-Nd-Pb-Hf isotopic and geochemical data of volcanic and intrusive rocks in Laoshankou show that the calc-alkaline volcanic rocks were derived from a depleted mantle wedge metasomatized by slab-derived fluids and the variable lithofacies were generated mainly through fractional crystallization. The biotite diorite is proposed to be the product of fractional crystallization from parental basaltic magmas with only minor assimilation of juvenile lower crust, whereas the quartz syenites are proposed to be the product of a depleted mantle wedge metasomatized by slab-derived fluids and subducted sediments-derived melts with minor crustal contamination.
(3) From 381 to 376 Ma the northern margin of East Junggar formed in a subduction related island arc environment rather than continental margin arc.

(4) The arc-related Late Paleozoic magmatism and mineralization on the northern margin of East Junggar were formed by the southward subduction of the Kuerti-Erqis Ocean (a branch of Paleo-Asian Ocean) lithosphere beneath the Junggar plate.
(5) There is considerable potential to find a Late Paleozoic Fe-Cu-Au metallogenic belt together with the porphyry Cu mineralization in the East Junggar.

Supplementary data to this article can be found online at http://dx.doi.org/10.1016/j.lithos.2016.08.021.

Acknowledgments

This study was supported by funds from the Chinese National Basic Research 973 Program (2014CB440802), Creative and Interdisciplinary Program, CAS (Y433131A07) and the Geogical Survey of China (Project 1212011140056). We thank Prof. Jinlong Ma, Prof. Xianglin Tu and Dr. Congying Li for support in the State Key Laboratory of Isotope Geochemistry, Guangzhou Institute of Geochemistry, Chinese Academy of Sciences. Long Chen and Zhenjiang Liu are warmly thanked for their hospitality and help during the authors' stay in Qinghe County, China, over the years. Prof. Yuquan Zhang, Dr. Jinsheng Han, Weifeng Zhang, Dengfeng Li, Jing Fang, Liandang Zhao, Hongjun Jiang, Chengming Wang and Wanjian Lu are acknowledged for their constructive and insightful discussions that generated many ideas. The manuscript benefited significantly from critical reviews and insightful comments by two anonymous reviewers. Detailed editorial suggestions from Sun.-Lin Chung also helped improve the quality of the paper.

This is contribution No.IS-2292 from GIGCAS.

References

Andersen, T., 2002. Correction of common lead in U–Pb analyses that do not report 204Pb. Chemical Geology 192, 59–79.
Arculus, R.J., Powell, R., 1986. Source component mixing in the regions of arc magma generation. Journal of Geophysical Research: Solid Earth (1978–2012) 91, 5913–5926.
Bai, M., 1996. Ertix active fault zone. Xinjiang Geology 14, 127–134 (in Chinese with English abstract).
Baxter, S., Feely, M., 2002. Magma mixing and mingling textures in granitoids: examples from the Galway Granite, Connemara, Ireland. Mineralogy and Petrology 76, 63–74.
Belousova, E., Griffin, W.L., O'reilly, S.Y., Fisher, N., 2002. Igneous zircon: trace element composition as an indicator of source rock type. Contributions to Mineralogy and Petrology 143, 602–622.
Black, L.P., Kamo, S.L., Allen, C.M., Aleinikoff, J.N., Davis, D.W., Korsch, R.J., Foudoulis, C., 2003. TEMORA 1: a new zircon standard for Phanerozoic U–Pb geochronology. Chemical Geology 200, 155–170.
Blichert-Toft, J., Albarède, F., 1997. The Lu-Hf isotope geochemistry of chondrites and the evolution of the mantle–crust system. Earth and Planetary Science Letters 148, 243–258.
Brown, G.C., Thorpe, R.S., Webb, P.C., 1984. The geochemical characteristics of granitoids in contrasting arcs and comments on magma sources. Journal of the Geological Society 141, 413–426.
Cai, K., Sun, M., Yuan, C., Zhao, G., Xiao, W., Long, X., Wu, F., 2010. Geochronological and geochemical study of mafic dykes from the northwest Chinese Altai: Implications for petrogenesis and tectonic evolution. Gondwana Research 18, 638–652.
Castillo, P.R., 2006. An overview of adakite petrogenesis. Chinese Science Bulletin 51, 257–268.
Chai, F., Yang, F., Liu, F., Geng, X., Lu, S., Jiang, L., Zang, M., Chen, B., 2012. Geochronology and genesis of volcanic rocks in Beitashan Formation at the northern margin of the Junggar, Xinjiang. Acta Petrologica Sinica 28, 2183–2198 (in Chinese with English abstract).
Chen, B., Jahn, B.M., 2004. Genesis of post-collisional granitoids and basement nature of the Junggar Terrane, NW China: Nd-Sr isotope and trace element evidence. Journal of Asian Earth Sciences 23, 691–703.
Chen, H.Y., Cooke, D.R., Baker, M.J., 2013. Mesozoic iron oxide copper-gold mineralization in the Central Andes and the Gondwana Supercontinent breakup. Economic Geology 108, 37–44.
Condie, K.C., 1989. Geochemical changes in baslts and andesites across the Archean-Proterozoic boundary: identification and significance. Lithos 23, 1–18.
Davies, J.H., von Blanckenburg, F., 1995. Slab breakoff: a model of lithosphere detachment and its test in the magmatism and deformation of collisional orogens. Earth and Planetary Science Letters 129, 85–102.
Defant, M.J., Drummond, M.S., 1990. Derivation of some modern arc magmas by melting of young subducted lithosphere. Nature 347, 662–665.
Ersoy, Y., Helvacı, C., 2010. FC–AFC–FCA and mixing modeler: A Microsoft® Excel© spreadsheet program for modeling geochemical differentiation of magma by crystal fractionation, crustal assimilation and mixing. Computers & Geosciences 36, 383–390.
Green, T.H., 1995. Significance of Nb/Ta as an indicator of geochemical processes in the crust–mantle system. Chemical Geology 120, 347–359.
Green, T.H., Ringwood, A., 1968. Genesis of the calc-alkaline igneous rock suite. Contributions to Mineralogy and Petrology 18, 105–162.
Griffin, W., Pearson, N., Belousova, E., Jackson, S., Van Achterbergh, E., O'Reilly, S.Y., Shee, S., 2000. The Hf isotope composition of cratonic mantle: LAM-MC-ICPMS analysis of zircon megacrysts in kimberlites. Geochimica et Cosmochimica Acta 64, 133–147.
Han, B.F., Wang, S.G., Jahn, B.M., Hong, D.W., Kagami, H., Sun, Y.L., 1997. Depleted-mantle source for the Ulungur River A-type granites from North Xinjiang, China: geochemistry and Nd–Sr isotopic evidence, and implications for Phanerozoic crustal growth. Chemical Geology 138, 135–159.
Hastie, A.R., Kerr, A.C., Pearce, J.A., Mitchell, S.F., 2007. Classification of altered volcanic island arc rocks using immobile trace elements: development of the Th Co discrimination diagram. Journal of Petrology 48, 2341–2357.
Hofmann, A.W., 1988. Chemical differentiation of the Earth: the relationship between mantle, continental crust, and oceanic crust. Earth and Planetary Science Letters 90, 297–314.
Hollings, P., Kerrich, R., 2000. An Archean arc basalt–Nb-enriched basalt–adakite association: the 2.7 Ga Confederation assemblage of the Birch–Uchi greenstone belt, Superior Province. Contributions to Mineralogy and Petrology 139, 208–226.
Huang, H., Zhang, Z., Santosh, M., Zhang, D., 2014. Geochronology, geochemistry and metallogenic implications of the Boziguo'er rare metal-bearing peralkaline granitic intrusion in South Tianshan, NW China. Ore Geology Reviews 61, 157–174.
Jahn, B.M., Wu, F., Chen, B., 2000. Massive granitoid generation in Central Asia: Nd isotope evidence and implication for continental growth in the Phanerozoic. Episodes 23, 82–92.
Kay, R.W., Kay, S.M., 1993. Delamination and delamination magmatism. Tectonophysics 219, 177–189.
Kaygusuz, A., Arslan, M., Siebel, W., Sipahi, F., İlbeyli, N., Temizel, İ., 2014. LA-ICP MS zircon dating, whole-rock and Sr–Nd–Pb–O isotope geochemistry of the Camiboğazı pluton, Eastern Pontides, NE Turkey: Implications for lithospheric mantle and lower crustal sources in arc-related I-type magmatism. Lithos 192-195, 271–290.
Ketchum, K.Y., Heaman, L.M., Bennett, G., Hughes, D.J., 2013. Age, petrogenesis and tectonic setting of the Thessalon volcanic rocks, Huronian Supergroup, Canada. Precambrian Research 233, 144–172.
Li, H., Chen, F., 2004. Isotopic geochronology of regional mineralization in Xinjiang, NW China. Geological Publishing House, Beijing (in Chinese with English abstract).
Li, Q., Zhang, Z., Geng, X., Li, C., Liu, F., Chai, F., Yang, F., 2014. Geology and geochemistry of the Qiaoxiahala Fe–Cu–Au deposit, Junggar region, northwest China. Ore Geology Reviews 57, 462–481.
Li, Q., Lu, S., Yang, F., Geng, X., Chai, F., 2015. Geological characteristics and genesis of the Laoshankou Fe-Cu-Au deposit in Junggar, Xinjiang, Central Asian Orogenic Belt. Ore Geology Reviews 68, 59–78.
Liang, X., Wei, G., Li, X., Liu, Y., 2003. Precise measurement of 143Nd/144Nd and Sm/Nd ratios using multiple-collectors inductively coupled plasma-mass spectrometer (MC-ICPMS). Geochimica 32, 91–96 (in Chinese with English abstract).
Liu, X., Liu, W., 2014. Source characteristics and tectonic setting of the Early and Middle Devonian volcanic rocks in the North Junggar, Northwest China: Insights from Nd–Sr isotopes and geochemistry. Lithos 184, 27–41.
Liu, Y., Gao, S., Hu, Z., Gao, C., Zong, K., Wang, D., 2010. Continental and Oceanic Crust Recycling-induced Melt-Peridotite Interactions in the Trans-North China Orogen: U–Pb Dating, Hf Isotopes and Trace Elements in Zircons from Mantle Xenoliths. Journal of Petrology 51, 537–571.
Liu, W., Liu, X.J., Liu, L.J., 2013. Underplating generated A- and I-type granitoids of the East Junggar from the lower and the upper oceanic crust with mixing of mafic magma: Insights from integrated zircon U–Pb ages, petrography, geochemistry and Nd–Sr–Hf isotopes. Lithos 179, 293–319.
Long, X., Yuan, C., Sun, M., Safonova, I., Xiao, W., Wang, Y., 2012. Geochemistry and U–Pb detrital zircon dating of Paleozoic graywackes in East Junggar, NW China: insights into subduction–accretion processes in the southern Central Asian Orogenic Belt. Gondwana Research 21, 637–653.
Lu, S., Yang, F., Chai, F., Zhang, X., Jiang, L., Liu, F., Zhang, Z., Geng, X., Ouyang, L., 2012. Zircon U–Pb dating for intrusions in Laoshankou ore district in Northern Margin of East Junggar and their significances. Geological Review 58, 149–164 (in Chinese with English abstract).
Lu, S., Yang, F., Chai, F., Geng, X., 2013. Geochemical features of granitoids in Laoshankou ore district on Northern Margin of East Junggar, Xinjiang. Geological Review 59, 971–982 (in Chinese with English abstract).
Ludwig, K.R., 2003. User's manual for Isoplot 3.00: a geochronological toolkit for Microsoft Excel. Berkeley Geochronology Center, Special Publication No.4a, Berkeley, California.
Meschede, M., 1986. A method of discriminating between different types of mid-ocean ridge basalts and continental tholeiites with the Nb-Zr-Y diagram. Chemical Geology 56, 207–218.
Miyashiro, A., Shido, F., 1975. Tholeiitic and calc-alkalic series in relation to the behaviors of titanium, vanadium, chromium, and nickel. American Journal of Science 275, 265–277.
Münker, C., Wörner, G., Yogodzinski, G., Churikova, T., 2004. Behaviour of high field strength elements in subduction zones: constraints from Kamchatka–Aleutian arc lavas. Earth and Planetary Science Letters 224, 275–293.
Pearce, J.A., 1982. Trace element characteristics of lavas from destructive plate boundaries. Andesites 528–548.
Pearce, J., Peate, D., 1995. Tectonic implications of the composition of volcanic arc magmas. Annual Review of Earth and Planetary Sciences 23, 251–286.

Pearce, J.A., Harris, N.B., Tindle, A.G., 1984. Trace element discrimination diagrams for the tectonic interpretation of granitic rocks. Journal of Petrology 25, 956–983.
Petford, N., Atherton, M., 1996. Na-rich partial melts from newly underplated basaltic crust: the Cordillera Blanca Batholith, Peru. Journal of Petrology 37, 1491–1521.
Plank, T., Langmuir, C.H., 1998. The chemical composition of subducting sediment and its consequences for the crust and mantle. Chemical Geology 145, 325–394.
Rapp, R.P., Watson, E.B., 1995. Dehydration melting of metabasalt at 8–32 kbar: implications for continental growth and crust–mantle recycling. Journal of Petrology 36, 891–931.
Richards, J.P., Kerrich, R., 2007. Special paper: adakite-like rocks: their diverse origins and questionable role in metallogenesis. Economic Geology 102, 537–576.
Rudnick, R., Gao, S., 2003. Composition of the continental crust. Treatise on Geochemistry 3, 1–64.
Scherer, E., Münker, C., Mezger, K., 2001. Calibration of the lutetium-hafnium clock. Science 293, 683–687.
Schiano, P., Clocchiatti, R., Shimizu, N., Maury, R., Jochum, K., Hofmann, A., 1995. Hydrous, silica-rich melts in the sub-arc mantle and their relationship with erupted arc lavas. Nature 377, 595–600.
Segal, I., Halicz, L., Platzner, I.T., 2003. Accurate isotope ratio measurements of ytterbium by multiple collection inductively coupled plasma mass spectrometry applying erbium and hafnium in an improved double external normalization procedure. Journal of Analytical Atomic Spectrometry 18, 1217–1223.
Sengor, A.M.C., Natalin, B.A., 1996. Paleotectonics of Asia: fragments of a synthesis. In: Yin, A., Harrison, T.M. (Eds.), The tectonic evolution of Asia. Cambridge University Press, Cambridge, pp. 486–641.
Sengor, A.M.C., Natalin, B.A., Burtman, V.S., 1993. Evolution of the Altaid tectonic collage and Paleozoic crustal growth in Eurasia. Nature 364, 299–307.
Sillitoe, R.H., 2003. Iron oxide-copper-gold deposits: an Andean view. Mineralium Deposita 38, 787–812.
Stern, C.R., Kilian, R., 1996. Role of the subducted slab, mantle wedge and continental crust in the generation of adakites from the Andean Austral Volcanic Zone. Contributions to Mineralogy and Petrology 123, 263–281.
Sun, S., McDonough, W.F., 1989. Chemical and isotopic systematics of oceanic basalts: implications for mantle composition and processes. Geological Society, London, Special Publications 42, 313–345.
Sun, M., Yuan, C., Xiao, W., Long, X., Xia, X., Zhao, G., Lin, S., Wu, F., Kroener, A., 2008. Zircon U–Pb and Hf isotopic study of gneissic rocks from the Chinese Altai: Progressive accretionary history in the early to middle Palaeozoic. Chemical Geology 247, 352–383.
Temizel, I., Arslan, M., Ruffet, G., Peucat, J.J., 2012. Petrochemistry, geochronology and Sr-Nd isotopic systematics of the Tertiary collisional and post-collisional volcanic rocks from the Ulubey (Ordu) area, eastern Pontide, NE Turkey: Implications for extension-related origin and mantle source characteristics. Lithos 128, 126–147.
Thirlwall, M., Smith, T., Graham, A., Theodorou, N., Hollings, P., Davidson, J., Arculus, R., 1994. High field strength element anomalies in arc lavas: source or process? Journal of Petrology 35, 819–838.
Tiepolo, M., Vannucci, R., Oberti, R., Foley, S., Bottazzi, P., Zanetti, A., 2000. Nb and Ta incorporation and fractionation in titanian pargasite and kaersutite: crystal–chemical constraints and implications for natural systems. Earth and Planetary Science Letters 176, 185–201.
Wan, B., Zhang, L., 2006. Sr-Nd-Pb isotope geochemistry and tectonic setting of Devonian polymetallic metallogenic belt on the Southern margin of Altaid, Xingjing. Acta Petrologica Sinica 22, 145–152 (in Chinese with English abstract).
Wan, B., Xiao, W., Zhang, L., Windley, B.F., Han, C., Quinn, C.D., 2011. Contrasting styles of mineralization in the Chinese Altai and East Junggar, NW China: implications for the accretionary history of the southern Altaids. Journal of the Geological Society 168, 1311–1321.
Wang, T., Hong, D., Jahn, B.M., Tong, Y., Wang, Y., Han, B., Wang, X., 2006. Timing, petrogenesis, and setting of Paleozoic synorogenic intrusions from the Altai Mountains, northwest China: Implications for the Tectonic evolution of an accretionary orogen. Journal of Geology 114, 735–751.
Wang, T., Jahn, B.M., Kovach, V.P., Tong, Y., Hong, D.W., Han, B.F., 2009. Nd–Sr isotopic mapping of the Chinese Altai and implications for continental growth in the Central Asian Orogenic Belt. Lithos 110, 359–372.
Wang, Y., Wang, J., Wang, L., Long, L., Tang, P., Liao, Z., Zhang, H., 2011. Discovery of Tuerkubantao ophiolitic melange in Xinjiang and its significance. Earth Science Frontiers 18, 151–165 (in Chinese with English abstract).
Wang, Y., Wang, J., Long, L., Zou, T., Wang, L., 2012. Tectonic evolution stages of northern Xinjiang and tectonic types of porphyryepithermal deposits. Geology of China 39, 695–716 (in Chinese with English abstract).
White, W., Hofmann, A., 1982. Sr and Nd isotope geochemistry of oceanic basalts and mantle evolution. Nature 296, 821.
Williams, P.J., Barton, M.D., Johnson, D.A., Fontboté, L., De Haller, A., Mark, G., Oliver, N.H., Marschik, R., 2005. Iron oxide copper-gold deposits: Geology, space–time distribution, and possible modes of origin. Economic Geology 371–405.
Wilson, B.M., 1989. Igneous petrogenesis a global tectonic approach. Springer.
Winchester, J., Floyd, P., 1977. Geochemical discrimination of different magma series and their differentiation products using immobile elements. Chemical Geology 20, 325–343.
Windley, B.F., Kroner, A., Guo, J., Qu, G., Li, Y., Zhang, C., 2002. Neoproterozoic to Paleozoic geology of the Altai orogen, NW China: New zircon age data and tectonic evolution. Journal of Geology 110, 719–737.
Wu, B., He, G., Wu, T., Li, H., Luo, H., 2006. Discovery of the Buergen ophiolitic mélange belt in Xinjiang and its tectonic significance. Geology in China 33, 476–486 (in Chinese with English abstract).
Wu, G., Dong, L., Xue, C., 2008. Main porphyry copper ore belt in Northern Xinjiang. Geological Publishing House, Beijing (in Chinese).
Wyman, D., Ayer, J., Devaney, J., 2000. Niobium-enriched basalts from the Wabigoon subprovince, Canada: evidence for adakitic metasomatism above an Archean subduction zone. Earth and Planetary Science Letters 179, 21–30.
Xiao, W., Han, C., Yuan, C., Sun, M., Lin, S., Chen, H., Li, Z., Li, J., Sun, S., 2008. Middle Cambrian to Permian subduction-related accretionary orogenesis of Northern Xinjiang, NW China: Implications for the tectonic evolution of central Asia. Journal of Asian Earth Sciences 32, 102–117.
Xu, J., Mei, H., Yu, X., Bai, Z., Niu, H., Chen, F., Zhen, Z., Wang, Q., 2001. Adakites related to subduction in the northern margin of Junggar arc for the Late Paleozoic: Products of slab melting. Chinese Science Bulletin 46, 1312–1316.
Xu, X., Jiang, N., Li, X., Qu, X., Yang, Y., Mao, Q., Wu, Q., Zhang, Y., Dong, L., 2013. Tectonic evolution of the East Junggar terrane: Evidence from the Taheir tectonic window, Xinjiang, China. Gondwana Research 24, 578–600.
Xue, C., Zhao, Z., Wu, G., Dong, L., Feng, J., Zhang, Z., Zhou, G., Chi, G., Gao, J., 2010. The multiperiodic superimposed porphyry copper mineralization in Central Asian Tectonic Region: A case study of geology, geochemistry and chronology of Halasu copper deposit, Southeastern Altai, China. Earth Science Frontiers 17, 53–82 (in Chinese with English abstract).
Yakubchuk, A., 2004. Architecture and mineral deposit settings of the Altaid orogenic collage: a revised model. Journal of Asian Earth Sciences 23, 761–779.
Yang, F., Mao, J., Pirajno, F., Yan, S., Liu, G., Zhou, G., Zhang, Z., Liu, F., Geng, X., Guo, C., 2012a. A review of the geological characteristics and geodynamic setting of Late Paleozoic porphyry copper deposits in the Junggar region, Xinjiang Uygur Autonomous Region, Northwest China. Journal of Asian Earth Sciences 49, 80–98.
Yang, F., Zhang, Z., Liu, G., Qu, W., Zhang, L., Wei, G., Liu, F., Chai, F., 2012b. Geochronology of Yulekenhalasu porphyry copper deposit in northtern Junggar area, Xinjiang, China. Acta Petrologica Sinica 28, 2029–2042 (in Chinese with English abstract).
Zartman, R., Doe, B., 1981. Plumbotectonics—the model. Tectonophysics 75, 135–162.
Zhang, H., Niu, H., Terada, K., Yu, X., Sato, H., Ito, J., 2003a. Zircon SHRIMP U–Pb dating on plagiogranite from Kuerti ophiolite in Altay, North Xinjiang. Chinese Science Bulletin 48, 2231–2235.
Zhang, Z., Yan, S., Chen, B., Zhou, G., He, Y., Chai, F., He, L., Wan, Y., 2006. SHRIMP U–Pb zircon age of subduction granite in the north of East Junggar, Xinjiang. Chinese Science Bulletin 51, 1565–1574 (in Chinese).
Zhang, Z., Zhou, G., Kusky, T.M., Yan, S., Chen, B., Zhao, L., 2009. Late Paleozoic volcanic record of the Eastern Junggar terrane, Xinjiang, Northwestern China: major and trace element characteristics, Sr-Nd isotopic systematics and implications for tectonic evolution. Gondwana Research 16, 201–215.
Zindler, A., Hart, S., 1986. Chemical geodynamics. Annual Review of Earth and Planetary Sciences 14, 493–571.